Sinter Bonding of Mo_2FeB_2 Based Cermet onto Steel Substrate and Sintering of Boride Cermet–SiC Fiber Composites

A Thesis Submitted

in Partial Fulfillment of the Requirements

for the Degree of

MASTER OF TECHNOLOGY

by

Dhaval Rao
(Roll No. 9820602)

DEPARTMENT OF MATERIALS AND METALLURGICAL ENGINEERING
INDIAN INSTITUTE OF TECHNOLOGY, KANPUR

MAY, 2000

I.I.T. Kanpur.
Submitted on 24.5.2000

Certificate

This is to certify that the thesis entitled **"Sinter bonding of Mo_2FeB_2 based cermet onto steel substrate and sintering of boride cermet–SiC fiber composites"** Submitted by **Dhaval Rao (Roll No. 9820602)** has been carried out under my supervision and to the best of my knowledge has not been submitted elsewhere for degree.

Dr. G. S. Upadhyaya 24/5/2000

Professor
Department of Materials and Metallurgical Engineering
Indian Institute of Technology
Kanpur, India.

6 OCT 2000
CENTRAL LIBRARY
I. I. T., KANPUR
Acc. No. A 132011
TH
MME/2000/M
N18

A132011

Acknowledgment

I take this opportunity to express my deep gratitude to Prof. G. S. Upadhyaya under whose guidance and supervision, the present work is carried out. His precious guidance, intelligent critics and perpetual encouragement throughout the present research are deeply acknowledged. His dynamic personality will be source of inspiration throughout my career.

I extend my special thanks to Mr. Soni and Dr. Mungole for extending every possible help during my experimental work.

I am grateful to my lab mates Pradyot Datta, Mayadhar Debata and Ranjan for maintaining productive and lively atmosphere in the lab. Their valuable support and affection is deeply appreciated.

At last but not the least, I am thankful to all the staff of MME and ACMS, who helped me at occasions.

Dhaval Rao

Table of Contents

		Page No.
List of Tables		i
List of Figures		ii
Abstract		iv
Chapter 1	**Literature Review**	**1**
1.1	Introduction	1
1.2	Sintering of Boride Cermets	3
1.2.1	Criteria for Development of Boride Cermets	3
1.2.2	Reaction Boronizing Sintering	5
1.2.3	Mo_2FeB_2 based cermets	6
1.2.3.1	Phase Equilibria and Crystal Structure	6
1.2.3.2	Production Process	7
1.2.3.3	Properties	7
1.2.4	Sintering Behaviour of Mo_2FeB_2 Cermets	7
1.2.4.1	Thremogravimetric and Differential Thermal Analysis	7
1.2.4.2	Dilatometric Analysis	8
1.2.4.3	X-ray Diffraction Analysis	8
1.2.5	Effect of Various Alloying Additives	9
1.3	Sinter Bonding of Mo_2FeB_2 Based Cermet onto Steel Steel substrate	11
1.4	Scope of the Present Work	12
Chapter 2	**Experimental Procedure**	**13**
2.1	Raw Materials	13
2.1.1	Green KH-C50 Sheet	13
2.1.2	Steel Plate	14
2.1.3	Silicon Carbide Fibers	14
2.1.4	Aluminium Powder	14
2.1.5	Aluminium Bronze Powder	14
2.1.6	Copper Powder	15
2.1.7	Poly Vinyl Alcohol (PVA)	15
2.2	Sample Preparation Prior to Sintering	15
2.3	Debinding and Sintering	16
2.4	Densification Behaviour	18
2.4.1	Linear and Volumetric Shrinkage	18

2.4.2 Total Sintered Porosity 18
2.5 Mechanical Properties 19
2.5.1 Vickers Macrohardness 20
2.5.2 Vickers Microhardness 20
2.5.3 Ultimate Tensile Strength 21
2.5.4 Transverse Rupture Strength 21
2.6 Microstructural Studies 22
2.6.1 Optical Microscopy 22
2.6.2 Scanning Electron Microscopy 22
2.6.3 Boride Grain Size Measurement 23
2.7 X-ray Diffraction Analysis 23
2.8 Electron Probe Micro Analysis 24

Chapter 3 Experimental Results 25
3.1 Sintering of Boride Cermet 25
3.1.1 Densification Behaviour 25
3.1.2 Mechanical Properties 26
3.1.3 X-ray diffraction Analysis 26
3.1.4 Optical Microstructure and SEM Fractography 27
3.1.5 Grain Size Measurement 28
3.2 Sinter Bonding of Boride Cermet onto Steel Substrate 29
3.2.1 Densification Behaviour 29
3.2.1.1 Total Sintered Porosity 29
3.2.1.2 Dimensional Changes 29
3.2.2 Ultimate Tensile Strength 30
3.2.3 Microhardness 30
3.2.4 EPMA Study of cermet / steel Diffusion Zone 31
3.2.5 Optical Microstructure and SEM Fractography 31
3.3 Layered boride cermet composite using SiC Fibers 33
3.3.1 Densification Behaviour 33
3.3.1.1 Total Sintered Porosity 33
3.3.1.2 Dimensional Changes 34
3.3.2 Transverse Rupture Strength 34
3.3.3 Microhardness 35
3.3.4 Optical Microstructure and SEM Fractography. 36

Chapter 4 Discussion 38
4.1 Sintering of Boride Cermet (KH-C50) 38
4.1.1 Interlamellar Binder (PVA) 38
4.1.2 Number of Boride Cermet Layer 39

4.1.3 Sintering Atmospheres and Cycles 39
4.1.4 X-ray Diffraction Analysis 41
4.2 Sinter bonding of Boride Cermet onto Steel Substrate 41
4.2.1 Densification Behaviour 41
4.2.2 Mechanical Properties 43
4.2.3 EPMA Study of cermet / Steel Diffusion Zone 43
4.2.4 Microstructural Studies 44
4.3 Sintering of layered Composites of Boride Cermet With SiC fibers 45
4.3.1 External Load During Sintering 45
4.3.2 Volume Fraction of SiC fibers 46
4.3.3 Interlamellar Metallic Additives 48
4.3.4 Sintering Atmospheres and Cycles 48
Chapter 5 Conclusions 50
References 52

List of Tables

Table 1.1 Angle of contact between refractory borides and molten metals [12].

Table 1.2 Crystallographic details including theoretical densities of various metallic-intermetallic binders and hard boride phases in ternary Fe-B-Mo alloy system [23].

Table 1.3 Properties of KH-C50 [29].

Table 1.4 The *insitu* chemical reactions occurring in KH-C50 during sintering cycle [12].

Table 2.1 The material composition of 'as received' KH-C50.

Table 2.2 The powder characteristics of the base material 'KH-C50' before green sheet formation.

Table 3.1 Results of hydrogen sintered layered boride cermet composites with or without SiC fibers.

Table 3.2 Results of vacuum sintered layered boride cermet composites with or without SiC fibers.

Table 3.3 Results of sinter bonded boride cermet layer onto steel substrates.

List of Figures

Figure 1.1 Schematic sequence of events expected in reaction sintering of Mo_2FeB_2 based cermet [2].

Figure 1.2 Isothermal Fe-B-Mo ternary equilibrium phase diagram at 1050 °C [23].

Figure1.3 Processing route employed for developing Mo_2FeB_2 based cermet by reaction sintering [3].

Figure 1.4(a) DTA plot of KH-C50 showing formation of liquid phase as an endothermic peak [22].

Figure 1.4(b) DTA plot of KH-C50 enlarged at lower temperature range [22].

Figure1.4(c) DTA plot of KH-C50 enlarged at higher temperature range [22].

Figure 1.5 TGA plot of KH-C50 showing decrease in weight upto 425 °C associated with debinding process [22].

Figure 1.6(a) Dilation plot of KH-C50 at lower temperature range. The nominal shrinkage above 405 °C and 670°C are associated with phase formation [22].

Figure 1.6(b) Dilation plot of KH-C50 at higher temperature range. The swelling occurs between 900 °C and 1150 °C. Shrinkage results above 1150 °C due to liquid phase formation [22].

Figure 1.7 Relative measure of various phases present at a given sintering temperature [12]

Figure 1.8 Dilation plot of KH-C50 sinter bonded onto 1018 steel substrate [22].

Figure 2.1 Time – temperature plot of sintering cycles 'A' and 'B'.

Figure 3.1 Properties of hydrogen and vacuum sintered boride cermet.

Figure 3.2 X-ray diffraction analysis of green and sintered boride cermet.

Figure 3.3 Optical micrographs of vacuum sintered boride cermet etched in different etching media (Sample 2, Table 3.2).
(a) as polished condition,
(b) etched with Nital
(c) etched with PPP reagent.

Figure 3.4 Optical micrographs of interface of hydrogen cycle 'A' sintered boride cermet.
(a) without PVA binder (Sample 1, Table 3.1)
(b) with PVA binder at interface during green compaction (Sample 2, Table 3.1).

Figure 3.5 SEM fractographs of boride cermet samples after TRS test.
(a) hydrogen cycle 'A' sintered (Sample 2, Table 3.1),
(b) hydrogen cycle 'B' sintered (Sample 12, Table 3.1),
(c) vacuum cycle 'A' sintered (Sample 1, Table 3.2),
(d) vacuum Cycle 'B' sintered (Sample 2, Table 3.2).

Figure 3.6 Variation of UTS of boride cermet cladded steel with volume percent of cermet phase.

Figure 3.7 Variation in the mechanical properties of steel plate used as substrate (after heating).

Figure 3.8 Microhardness variation in the sinter bonded cermet region from cermet / steel interface.

Figure 3.9 EPMA of sinter bonded cermet across cermet / steel diffusion zone.

Figure 3.10 Optical micrographs of sinter bonded boride cermet onto steel (sample 1, Table 3.3)
(a) cermet cladding,
(b) overall view cermet / steel interface,
(c) steel substrate.

Figure 3.11 SEM fractographs of sinter bonded boride cermet onto steel (Sample 1, Table 3.3) after tensile testing.
(a) cermet cladding,
(b) diffusion zone of cermet / steel interface,
(c) steel substrate.

Figure 3.12 Optical micrographs of sandwiched boride cermet layer of different thickness between two steel plates.
(a) and (b), Sample with thicker boride cermet layer between steel plates (Sample 2, Table 3.3).
(c) and (d), Sample with thinner boride cermet layer between steel plates (Sample3, Table 3.3).

Figure 3.13 SEM fractographs of sandwiched boride cermet layer between two steel plates (Sample 2, Table 3.3), after tensile testing.
(a) boride cermet region.
(b) diffusion zone of cermet / steel interface.

Figure 3.14 Variation of percentage porosity in the composites with volume percent of SiC fibers and sintering cycles.

Figure 3.15 Variation of linear shrinkage of the composites in fiber direction with volume percent of SiC fibers and sintering cycles.

Figure 3.16 Variation of TRS of composites with volume percent of SiC fibers and sintering cycles.

Figure 3.17 Variation of microhardness in 2 Vol. % SiC composite across the interface containing SiC fibers.

Figure 3.18 Optical micrographs of lamellar boride cermet composites containing different volume percent of SiC fibers.
(a) 2 % SiC, hydrogen sintered (Sample 6, Table 3.1),
(b) 4.4 % SiC, hydrogen sintered (Sample 5, Table 3.1),
(c) 2 % SiC, vacuum sintered (Sample 3, Table 3.2),
(d) 4.4 % SiC, vacuum sintered (Sample 4, Table 3.2).

Figure 3.19 SEM fractographs of lamellar composites containing different volume percent of SiC fibers and sintered in different atmosphere.
(a) 2 % SiC, hydrogen sintered (Sample 13, Table 3.1),
(b) 4.4 % SiC, hydrogen sintered (Sample 14, Table 3.1),
(c) 2 % SiC, vacuum sintered (Sample5 , Table 3.2),
(d) 4.4 % SiC, vacuum sintered (Sample 6, Table 3.2).

Figure 3.20 SEM fractographs of 2 vol. % SiC lamellar composites with and without interlayer metallic additive.

(a) no interlayer additive (Sample 6, Table 3.1),

(b) 2 vol. % aluminium-bronze as interlayer additive (Sample 8, Table 3.1).

Abstract

Reaction sintering is a unique process which utilizes the reactive nature of boron to develop ultra hard ternary borides (HR_A >85) coexisting with metal binder, which are difficult to fabricate otherwise. This process has dual role, *insitu* formation of hard phase through chemical reactions and densification via liquid phase sintering.

The current investigation monitors the composite making capabilities of Mo_2FeB_2 based model cermet (KH-C50). The effect of sintering atmospheres (hydrogen and vacuum) on the properties of the cermet has been investigated. It has been observed that vacuum sintered cermets have remarkably better densification than hydrogen sintered ones. The revised sintering cycle, having a 'Reduction Stage' at 1000 °C lasting 60 min., helped in achieving better densification in vacuum, but in hydrogen the results are not encouraging.

The sinter bonding process involves simultaneous densification and bonding of the cermet to the steel substrates. In the present investigation it has been observed that cermet cladding lowers the tensile strength of steel. EPMA study has been done to examine the concentration variation of different constituent near to cermet / steel diffusion zone.

The last section of the thesis deals with processing / property relationship of the layered composites of Mo_2FeB_2 based cermet with SiC fibers. The fibrous composites have more porosity than straight boride cermet.

CHAPTER –1

LITERATURE REVIEW

1.1 Introduction

Metal borides and their application in engineering materials have been intensively studied, and outstanding properties of borides documented [1]. Boron, borides and related compounds have unique bonding characteristics, structural peculiarities, and superior intrinsic properties [1]. These materials, especially transition metal borides posses high hardness, refractoriness, electrical conductivity, thermal conductivity and superior corrosion resistance. In spite of these impressive attributes, borides are late comers on scene and applications are limited. Processing and fabrication of borides by powder metallurgy involve many technological challenges. Poor sinterability and extreme brittleness are inherent in borides [2]. These restrict attainment of full density during sintering and adversely affects the corrosion and wear resistance properties. Additionally boron is highly reactive and forms a brittle third phase with transition metal during processing [2]. This deteriorates the strength of material.

A novel sintering technique, named Reaction Boronizing Sintering has been developed for liquid phase sintering of boride based cermets following *insitu* formation of ternary boride in binding metal matrix [2]. The boride based hard cermets were first commercially developed in Japan in early eighties by a firm named Toyo Kohan Co. Ltd., Tokyo. Three major variants of ternary boride based cermets are Mo_2FeB_2 based, meant for general wear resistant applications [3], WCoB based heat and wear resistant [4], and Mo_2NiB_2 based corrosion and wear resistant cermets [5].

Some of the wear resistant machine parts preferably require bimetallic structures with motive of partial wear resistance, strengthening, toughening, and cost reduction. It is very important to know the bonding feasibility and characteristics of the Mo_2FeB_2 based cermet to general coupling and strengthening materials. One of the important variant of reaction sintering is to sinter-bond these cermets onto steel substrates by heating laminated material to elevated temperatures [3]. The Mo_2FeB_2 based cermets find applications in harsh wear conditions such as injection molding screws, powder treatment equipment parts, metal forming and shaping tools, and hot metal extrusion dies.

Takagi et al's focus was to monitor the effects of various alloying additions, phase evolution, microstrutural evolution and subsequent testing of

properties, so as to widen application of the cermet. Sivaraman [22] has studied reaction and densification mechanisms involved in sinter bonding process.

1.2 Sintering of Boride Cermets

The development of boride based cermets is limited by its processing difficulties. Borides have high brittleness and poor sinterability, which adversely affects its densification. Epik [19] suggested use of powder metallurgy for borides as early as 1976. However, formation of cermet requires good wetting of borides by metal melt. The wettability of borides by metal melt was found to be poor due to high contact angle between the two [25]. This was attributed to negligible chemical reactions between the borides and metal melt. A summary of angle of contact between refractory borides and molten metal is tabulated in Table 1.1 [22].

1.2.1 Criteria for Development of Boride Cermets

It was observed that the wetting of borides by metals is directly related to their electronic and crystalline structure. Metals with filled *d* electrons exhibited poor wetting properties as compared with metals having unfilled *d* electrons. Additionally, it was observed that chemical reactions involving migrations of elements from the melt to the borides, displayed good wettability as compared to reactions involving migration of elements from the borides to metal melt.

Takagi et al [2] extensively observed chemical reactions between lower borides and the metal matrix resulting in formation of third phase consistent with attainment of stable sp^3 configuration. These third phase being highly brittle adversely affect the mechanical properties. For good wear, corrosion, and oxidation resistance at high temperatures, the stability of these borides is very important. The densification of these borides is limited by its high brittleness and poor sinterability. Hence solid state sintering is not an effective way of densifying borides. Liquid phase sintering provides a route through which full density can be attained without external pressure [26]. However, the melt employed has to wet the borides completely for sintering to occur. Takagi et al [2] summarized the important criteria for development of boride based cermet as

1. Selection of boride which can coexist with a metal matrix.
2. Prevention of formation of brittle third phase resulting due to chemical reaction between the borides and metal matrix.
3. Formation of liquid phase during the process to aid densification.
4. Restricting grain growth during high temperature sintering.

1.2.2 Reaction Boronizing Sintering

Reaction Boronizing is an innovative technique to consolidate hard brittle materials with low sinterability, in particular, ternary boride cermets. Takagi et al [2] described the basic principle of the new process as the enhancement of reaction between the boride and metal matrix to generate ternary boride coexisting with the metal matrix. This was followed by densification of cermet via liquid formation between ternary boride and the metal matrix. This technique of development of ternary boride cermets was extended for varying metal binders. Bagdi [23] did extensive study on partial replacement of costlier metal binder nickel by iron. The sequence of steps involved in the Reaction Boronizing Sintering is [2],

1. The starting raw materials consist of elemental and binary boride powders.
2. Heating to high temperatures resulting in *insitu* formation of ternary borides.
3. Formation of liquid due to chemical reaction between ternary boride and the metal matrix.
4. Densification through liquid phase sintering.

Fig.1.1 illustrates above steps schematically.

1.2.3 Mo_2FeB_2 Based Cermets

1.2.3.1 Phase Equilibria and Crystal Structures

The Mo_2FeB_2 has the tetragonal lattice configuration. The crystal structure is isotype with that of U_3Si_2 super structure. The isothermal cross section of the Fe-Mo-B at 1323 K (1050 °C) is shown in Fig.1.2 [23].

Various phases present in Mo-Fe-B ternary alloy system, their crystal structure, structure type, lattice parameters as reported are listed in Table 1.2 [23].

1.2.3.2 Production Process

Fig. 1.3 describes the production route for Mo_2FeB_2 based cermet. The Fe-Cr-B alloy powder is prepared by atomization. Boride powders such molybdenum boride, iron boride, and powders of iron, molybdenum, chromium, nickel etc. are used as raw materials. In this process it is not needed to prepare the Mo_2FeB_2 powder separately. The prescribed composition mixture is subjected to mixing and grinding in a wet ball mill, then dried, granulated and pressed and further sintering is performed under vacuum or reducing atmosphere at temperature of 1245 °C for 1.2 ks [2]. Sintered bodies are then ground according to needs and made into final products. Complex shaped products are machined at pre-sintering stage.

1.2.3.3 Material Properties

Table 1.3 gives a comprehensive look at various properties of fully sintered Mo_2FeB_2 based model cermet, being used in the present investigation.

1.2.4 Sintering Behaviour of Mo_2FeB_2 Based Cermets

Reaction sintering is an innovative process involving a series of *insitu* reactions leading to multiple phase formation. The densification of material proceeds through liquid phase sintering. The following section discusses the phase evolution during reaction sintering of Mo_2FeB_2 based model cermet being used in the present investigation.

1.2.4.1 Thermogravimetric and Differential Thermal Analysis

Thermogravimetric Analysis (TGA) and Differential Thermal Analysis (DTA) are used to study the heat and weight changes occurring when powder is heated. Fig. 1.4 (a)-(c) and Fig. 1.5 are the TGA and DTA plots for Mo_2FeB_2 based model material [22]. Fig. 1.4 (b) and (c) show a series of exothermic peaks at temperatures of 486 °C, 673 °C, and 1126 °C. Endothermic peaks are observed at temperatures of 1132 °C and 1166 °C. The peaks appearing at lower three temperatures are absent in cooling cycle. This indicates that the reactions during the process of attainment of the equilibrium phases are irreversible in nature.

The TGA plot in Fig. 1.5 shows a decrease in weight upto a temperature of 425 °C. This decrease in weight is attributed to volatilization of organic binder. There is a continuos decrease in weight at temperatures above 900 °C. This is due to inherent deoxidation of material activated by reducing elements like carbon (around 0.1%) present in the material [12].

1.2.4.2 Dilatometric Analysis

The dilation plot of Mo_2FeB_2 based model material is shown in Fig.1.6 (a) and (b) [22]. The shrinkage up to 400 °C is the result of particle rearrangement on burning out of Poly Vinyl Butyrl (PVB) binder used for green compaction. Fig 1.6 (b) shows a swelling above 900 °C up to 1150 °C, resulting due to formation of new phases by reactions during heating. A large shrinkage (of approximately 22 %) indicates formation of liquid phase.

The dilation analysis establishes that negligible densification (only 2 %) occurs through solid state sintering and major densification is through liquid phase sintering.

1.2.4.3 X-ray Diffraction Analysis

Fig. 1.7 is the bar chart showing relative intensities of the peaks of various phases at the temperature of interest. As evident from the figure, the relative intensity of molybdenum does not fall below 800 °C. The fall in its intensity above this temperature (around 1000 °C) is concurrent with the

appearance of Mo_2FeB_2 peaks. This can be attributed to the reaction between molybdenum and Fe_2B to form ternary boride. At the higher temperature, the substitutional element chromium reacts with Mo_2FeB_2 to form $(Mo, Fe, Cr)_3B_2$.

Based on the above analysis, the reactions involved in reaction sintering of Mo_2FeB_2 based cermet can be tabulated as in Table 1.4.

1.2.5 Effect of Various Alloying Additives

Takagi et al [3] used reaction sintering for the first time in development of Mo_2FeB_2 based cermet. The initial composition used was Fe-46.6Mo-5.4B-3 Ni-2Cr in weight percent. The formation of Mo_2FeB_2 was found to proceed through a series of *insitu* reactions. The liquid formation between the ternary boride and the matrix leads to instantaneous densification. Using X-ray diffraction studies presence of Fe_2B along with ternary boride in the final sintered part was observed.

Boron and residual carbon contents control the hardness of cermet. The transverse rupture strength (TRS) increases with decrease in hardness i.e. with lowering of boron content [3]. 0.1% residual carbon content is associated with the martensitic binder and a very small amount of austenite and M_6C phases. The ferrous binder changes from, ferritic to martensitic, with increasing residual carbon content. The ferritic binder and the increase of austenite and M_6C phases decrease the TRS. Hence about 0.1 weight % residual carbon is

considered to be optimal content to obtain the best combination of TRS and hardness [17]. Ando et al [12], monitored the effect of varying molybdenum content on the final mechanical properties of the sintered parts. They found that for molybdenum to boron ratio of 0.9, the properties obtained were best. No third phase formation was observed in the final sintered part. They also highlighted the importance of low heating rates through solid phase reaction stage, so that final densification proceeds similar to supersolidus liquid phase sintering. Takagi et al [9] postulated that TRS of Mo_2FeB_2 based hard alloy strongly depends not only on its molybdenum to boron atomic ratio but also on its chromium content. Third phase formation also found to decrease with increasing chromium content because of chromium substitution for molybdenum in the boride phase. Chromium addition offsets the liquid formation to higher temperature. It varies between 1200 °C to 1300 °C for different chromium additions.

Nickel additions were made to the system Fe-44.4Mo-5B by Takagi et al [11,18] to improve corrosion resistance, TRS and hardness. They reported that TRS increased to 2.24 GPa at nickel content of 2.5%, it then decreases with nickel content. However is maximum at 5.0% nickel with a value of 87 HR_A. Nickel is contained in the iron base binder phase, which changes from ferrite to martensite, to austenite with increasing Ni content.

1.3 Sinter Bonding of Mo_2FeB_2 Based Cermet onto Steel Substrate

The bonding between Mo_2FeB_2 based cermets and the steel substrate proceeds through formation of a eutectic melt of iron -boron at the interface. It is similar to Transient Liquid Phase Bonding (TLPB), except that in TLPB the liquid formed at interface is transitory. Further, there is a remnant interface at the completion of the sinter bonding process.

At the interface no pores are observed and thin diffusion layer indicates the formation of ideal bonding. Moreover this sinter bonding process conserves energy, since it reduces a process of heat treatment necessary in usual soldering and diffusion bonding processes. The thermal expansion coefficient for these cermets (9-12 X 10^{-6} / °C) is close to that of steel. This explains the realisation of bonding. Sinter bonding strength of the order of 400 MPa was obtained [24]. Observations also yield that surface roughness of the substrates has minor influence on the bonding strength [24].

Fig. 1.8 is the Dilation plot of Mo_2FeB_2 based cermet sinter bonded on to steel 1018 substrates [22]. The plot shows two distinct stages of shrinkage. The first stage (~ 20 %) occurs at 1210 °C while the second stage (~ 5 %) proceeds above 1240 °C. This amount of shrinkage is associated with liquid phase formation. The liquid formed at 1250 °C is persistent throughout the

sinter bonding process while the liquid formed at lower temperature is transient in nature.

1.4 Scope of the Present Work

The present work is an attempt to monitor the composite making capabilities of the Mo_2FeB_2 based cermets. In the first section thesis the effect various sintering parameters on the propeties of the straight boride cermet has been studied. In the next section, joining of Mo_2FeB_2 based cermet with steel (S-16) has been studied. There are many applications where bimetallic structure is of great significance, for the purpose of hardness, toughness, strength, wear and corrosion resistance, and of course cost reduction. Structure cladded with wear and corrosion resistant materials like Mo_2FeB_2 based cermet on some tough and cheap substrates can have wide areas of application.

In the second part of the thesis lamellar composites of SiC fibers with Mo_2FeB_2 based cermet has been described. Literature study reveals that it is for the first time such fiber reinforcement has been made on Mo_2FeB_2 based cermets.

Table 1.1 Angle of contact between refractory borides and molten metals [22].

Metal - Boride System	Contact or Wetting Angle, Degree
$Cu\text{-}ZrB_2$	138
$Cu\text{-}TiB_2$	136
$Cu\text{-}Mo_2B_5$	127
$Cu\text{-}Mo_2B_5$	127
$Al\text{-}ZrB_2$	107
$Al\text{-}CrB_2$	58
$Al\text{-}TiB_2$	114
$Fe\text{-}ZrB_2$	122
$FeTiB_2$	118
$Ni\text{-}Mo_2B_5$	75

Table 1.2 Crystallographic details including theoretical densities of various metallic-intermetallic binders and hard boride phases in the ternary Fe-B-Mo alloy system [23].

Phase	Crystal Structure	Structure type	Lattice Parameters, 10^{-10} m			Theoretical Density, Mg/m^3
			a	b	c	
α Fe	Cubic (BCC)	w	2.8604	-	-	7.8648
Mo	Cubic (BCC)	w	3.1472	-	-	10.2206
B	Tetragonal	B	10.1	-	14.28	2.366
MoFe	Tetragonal	CrFe	9.218	-	4.813	9.2439
Mo_6Fe_7	Hexagonal	W_6Fe_7	4.751	-	25.68	9.5913
Mo_2B	Tetragonal	Al_2Cu	5.547	-	4.739	9.2329
Mo_3B_2	Tetragonal	U_3Si_2	6.002	-	3.146	9.0673
MoB	Tetragonal	MoB	3.105	-	16.97	8.6671
MoB_2	Hexagonal	AlB_2	3.04	-	3.07	7.9445
MoB	Orthorhombic	CrB	3.16	8.61	3.08	8.4608
Mo_2B_5	Hexagonal	Mo_2B_5	3.011	-	20.93	7.4548
FeB	Orthorhombic	FeB	4.0587	5.5032	2.947	6.7025
Fe_2B	Tetragonal	Al_2Cu	5.099	-	4.24	7.3807
$MoFe_2B_4$	Orthorhombic	Ta_3B_4	3.128	12.7	2.984	7.0282
Mo_2FeB_4	Orthorhombic	Ta_3B_4	3.11	14.27	3.19	6.8253
Mo_2FeB_2	Tetragonal	U_3Si_2	5.782	-	3.148	8.4991

Table 1.3 Properties of KH-C50 [29].

Density	8.3 g/cm^3
Hardness	86 HR_A
Transverse Rupture Strength	230 kg/mm^2
Young's Modulus	3.3×10^4 kg/mm^2
Poisson's Ratio	0.27
Compressive Strength	380 - 480 kg/mm^2
Charpy Impact Test Value	0.4 - 1.1 kg.m
Fracture Toughness	7.7 - 21.1$MN/m^{1.5}$
Linear Thermal Expansion Coefficient	11.2×10^{-6} /°C
Thermal Conductivity	0.04 cal/cm.s.°C
Specific Heat	0.19 cal / g.°C
Specific Electric Resistance	75.2 μohm.cm

Table 1.4 The in situ chemical reaction occurring in 'KH-C50' during sintering cycle [12].

Temperature (°C)	**Reactions**
486	$Fe + FeB \rightarrow Fe_2B$
1126	$2Mo + 2Fe_2B \rightarrow Mo_2FeB_2$ (tetragonal) + 3Fe; Mo_2FeB_2 (tetragonal) --> (Mo, Fe, Cr)$_3B_2$ (tetragonal)
1132	$X + (1/z)\ M_xO_y \rightarrow (x/z)M + XO$ (Deoxidation by the reducing agents like carbon)
1180	$Fe + Fe_2B$ + (Mo,Fe, Cr)$_3B_2$ (tetragonal) --> Liquid + (Mo, Fe, Cr)$_3B_2$ (tetragonal)

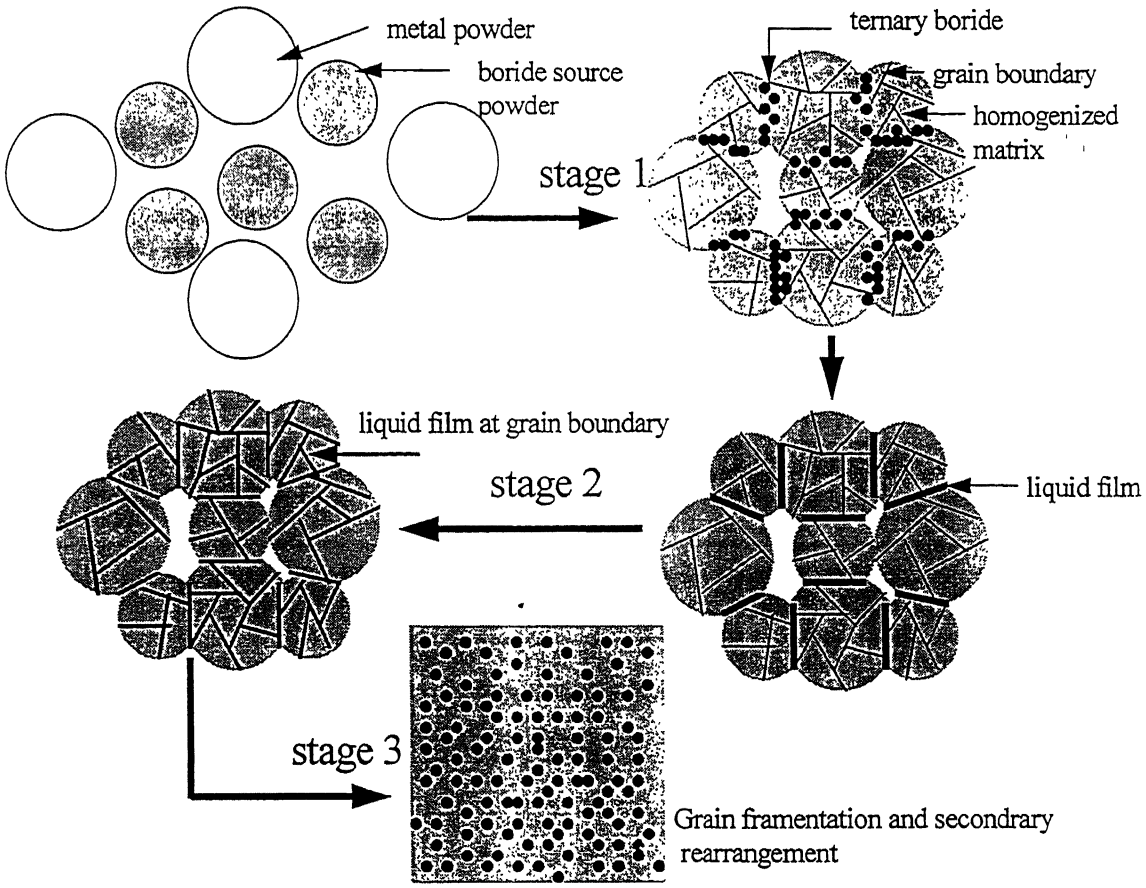

Figure 1.1 Schematic sequence of events expected in reaction sintering of Mo_2FeB_2 based cermets [2].

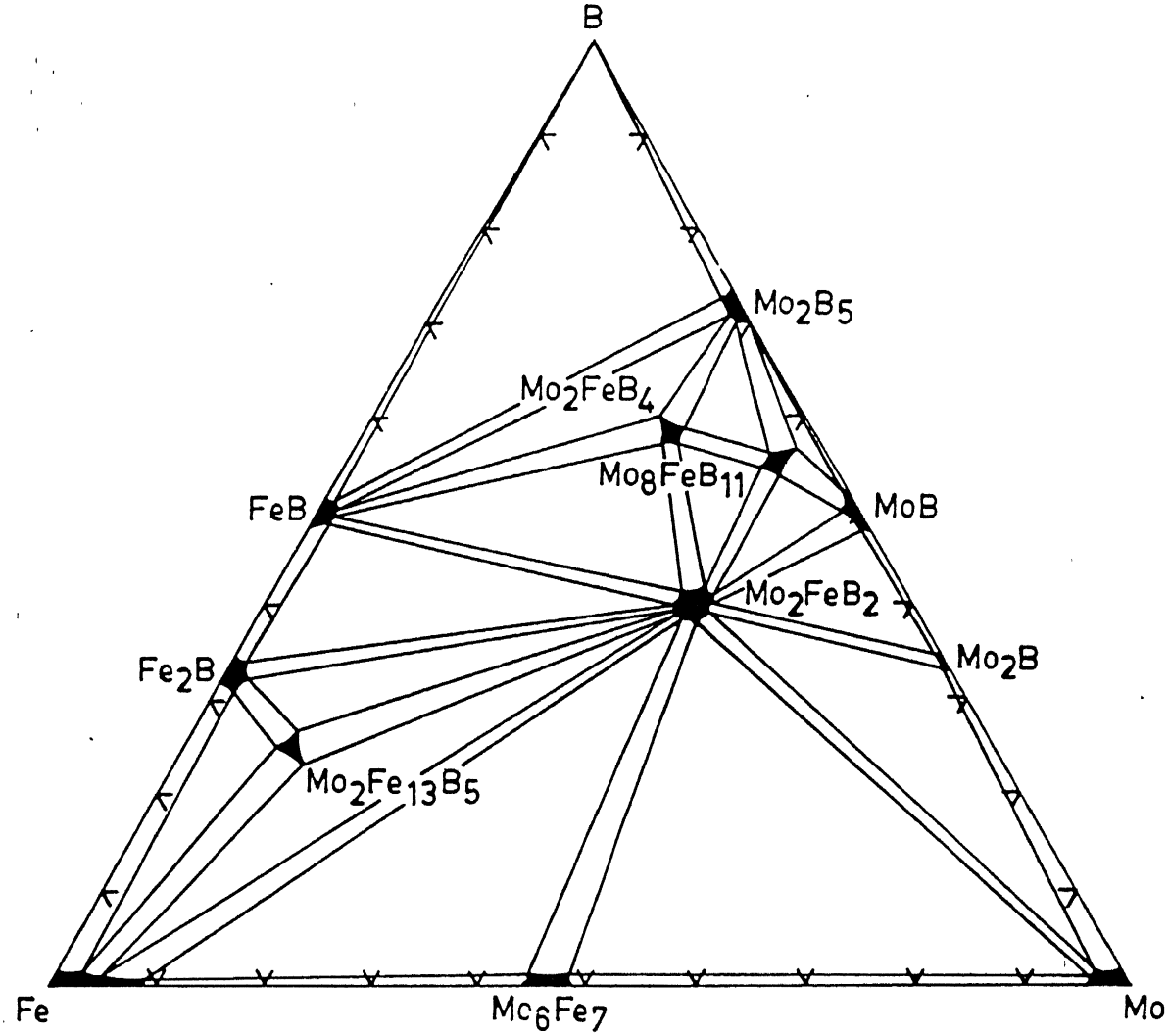

Figure 1.2 Isothermal Fe-B-Mo ternary equilibrium phase diagram at 1050 °C [23].

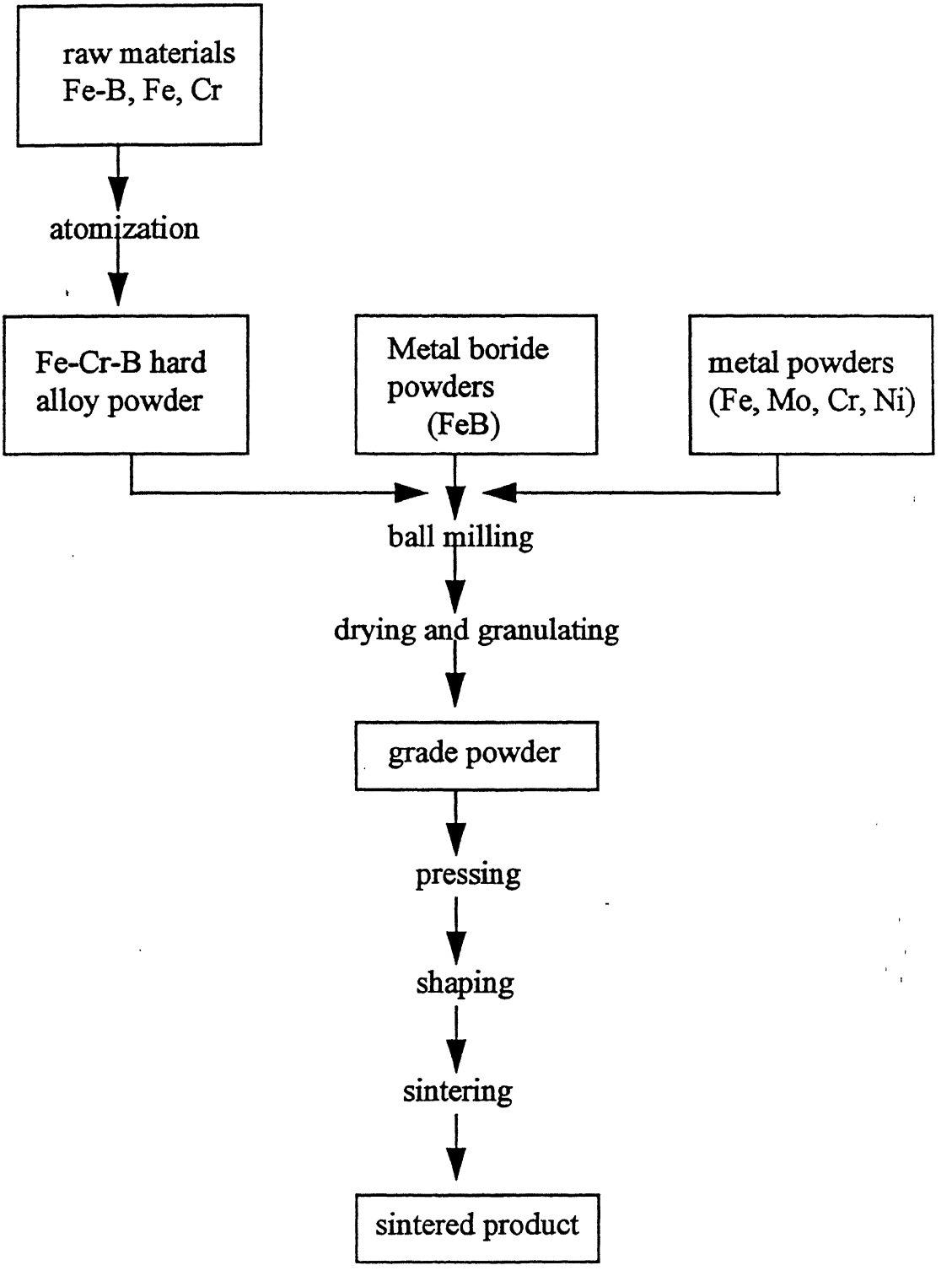

Figure1.3 Processing route employed for developing Mo_2FeB_2 based cermet by reaction sintering [3].

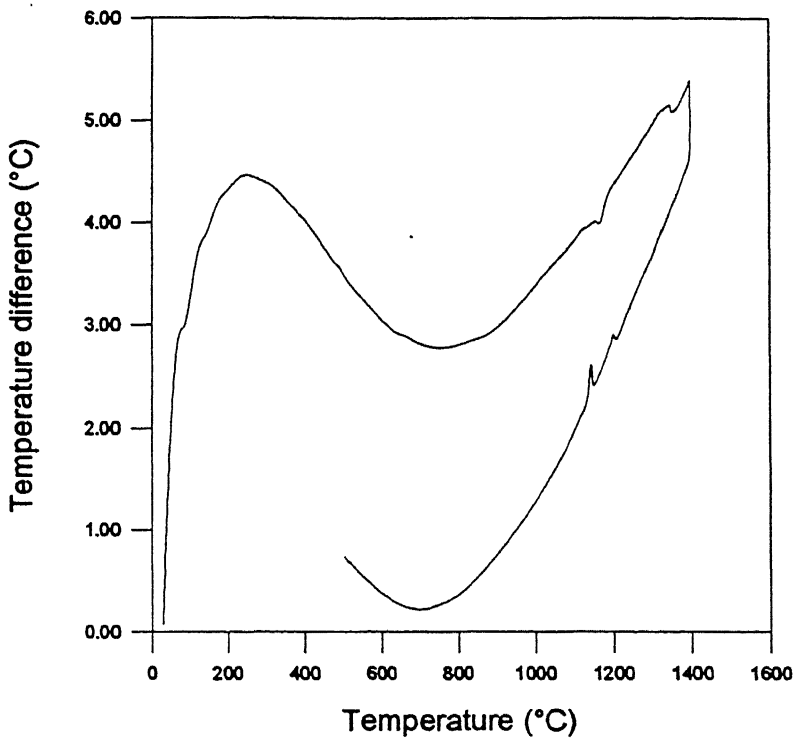

Figure 1.4(a) DTA plot of KH-C50 showing formation of liquid phase as an endothermic peak [22].

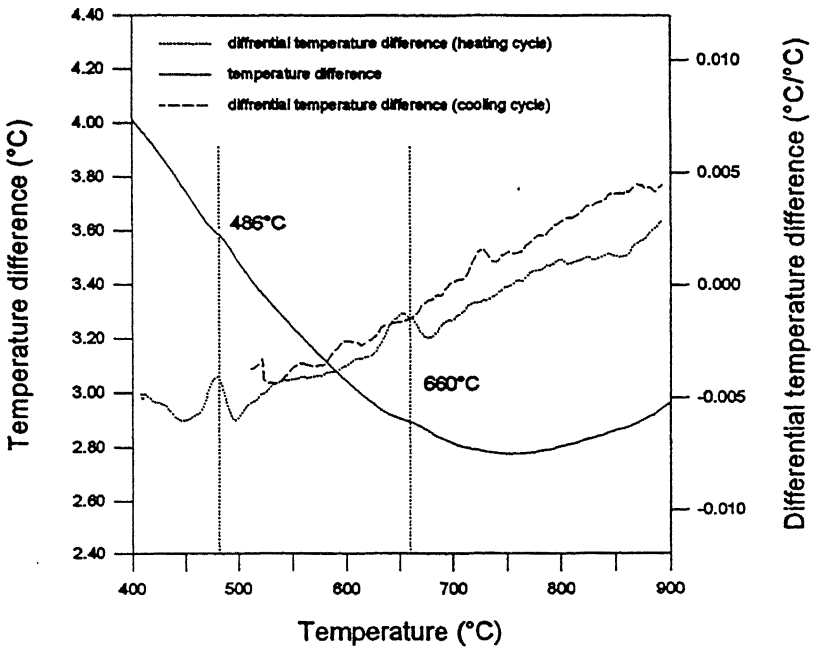

Figure 1.4(b) DTA plot of KH-C50 enlarged at lower temperature range [22].

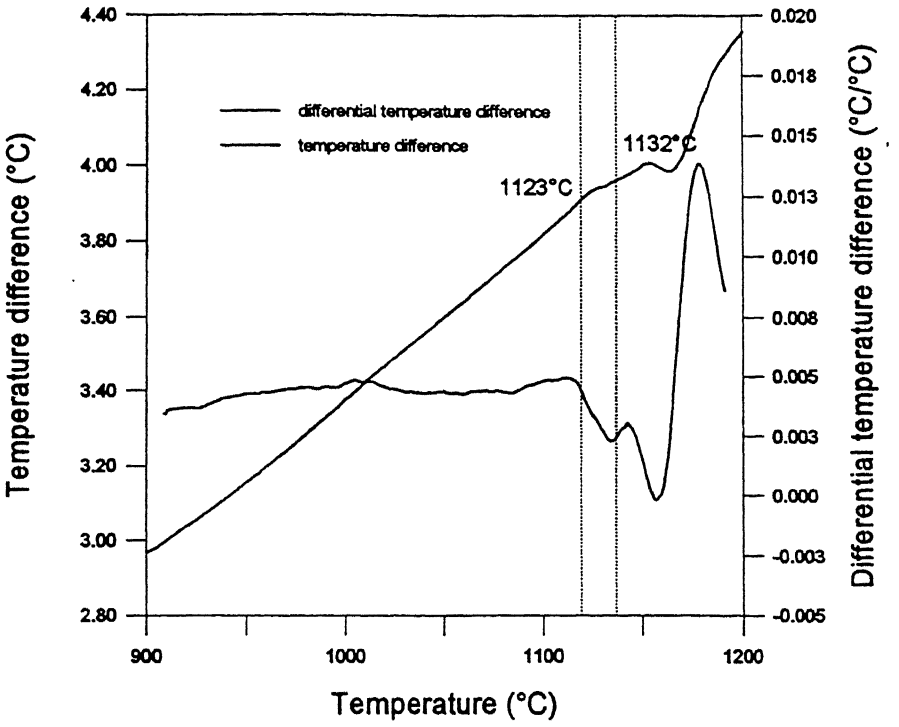

Figure1.4(c) DTA plot of KH-C50 enlarged at higher temperature range [22].

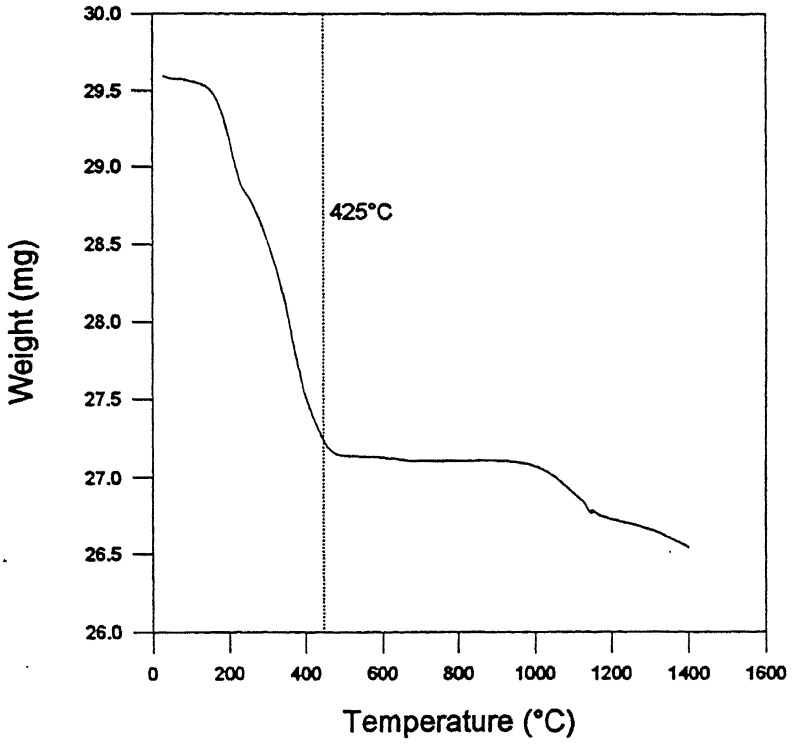

Figure 1.5 TGA plot of KH-C50 showing decrease in weight upto 425 °C associated with debinding process

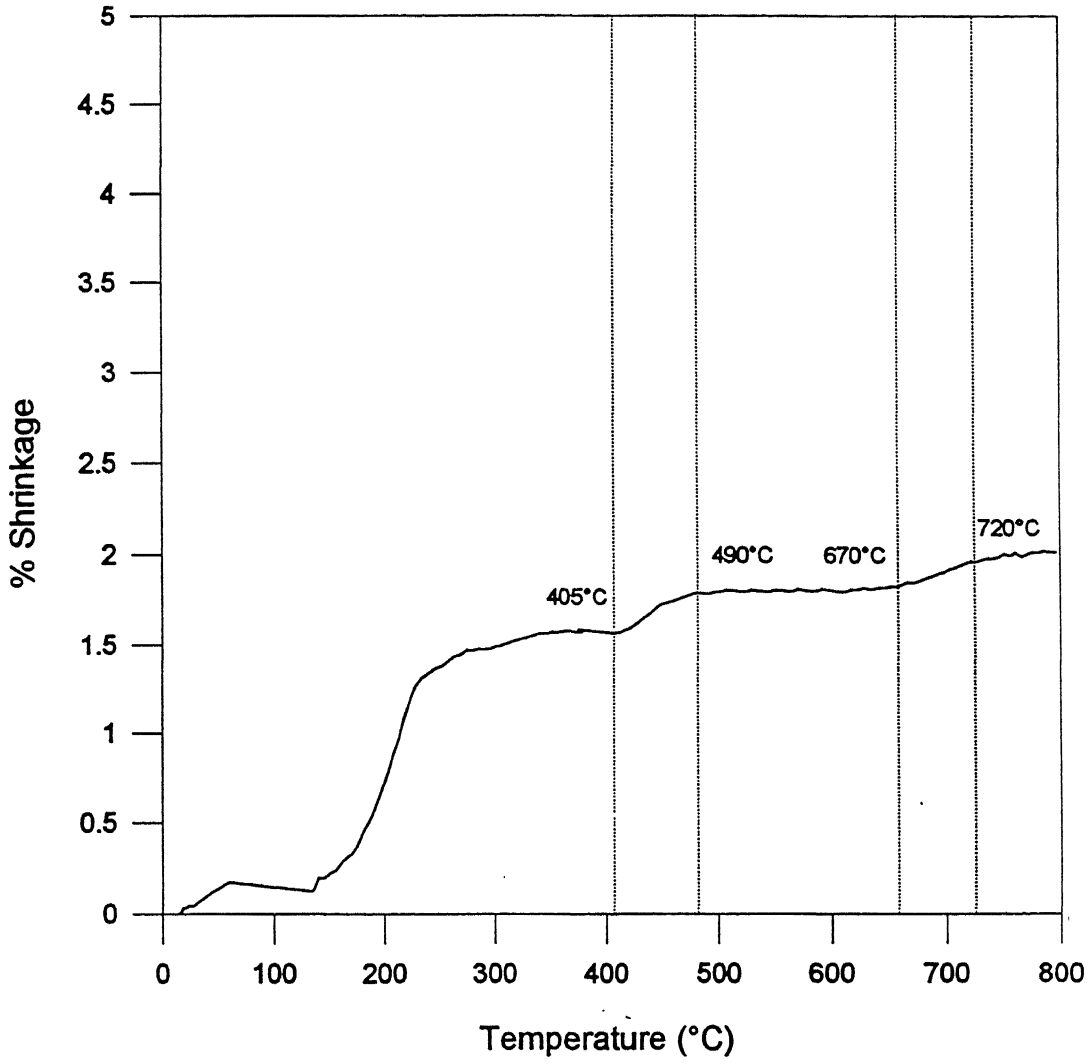

Figure 1.6(a) Dilation plot of KH-C50 showing nominal shrinkage above 405 °C and 670°C associated with phase formation [22].

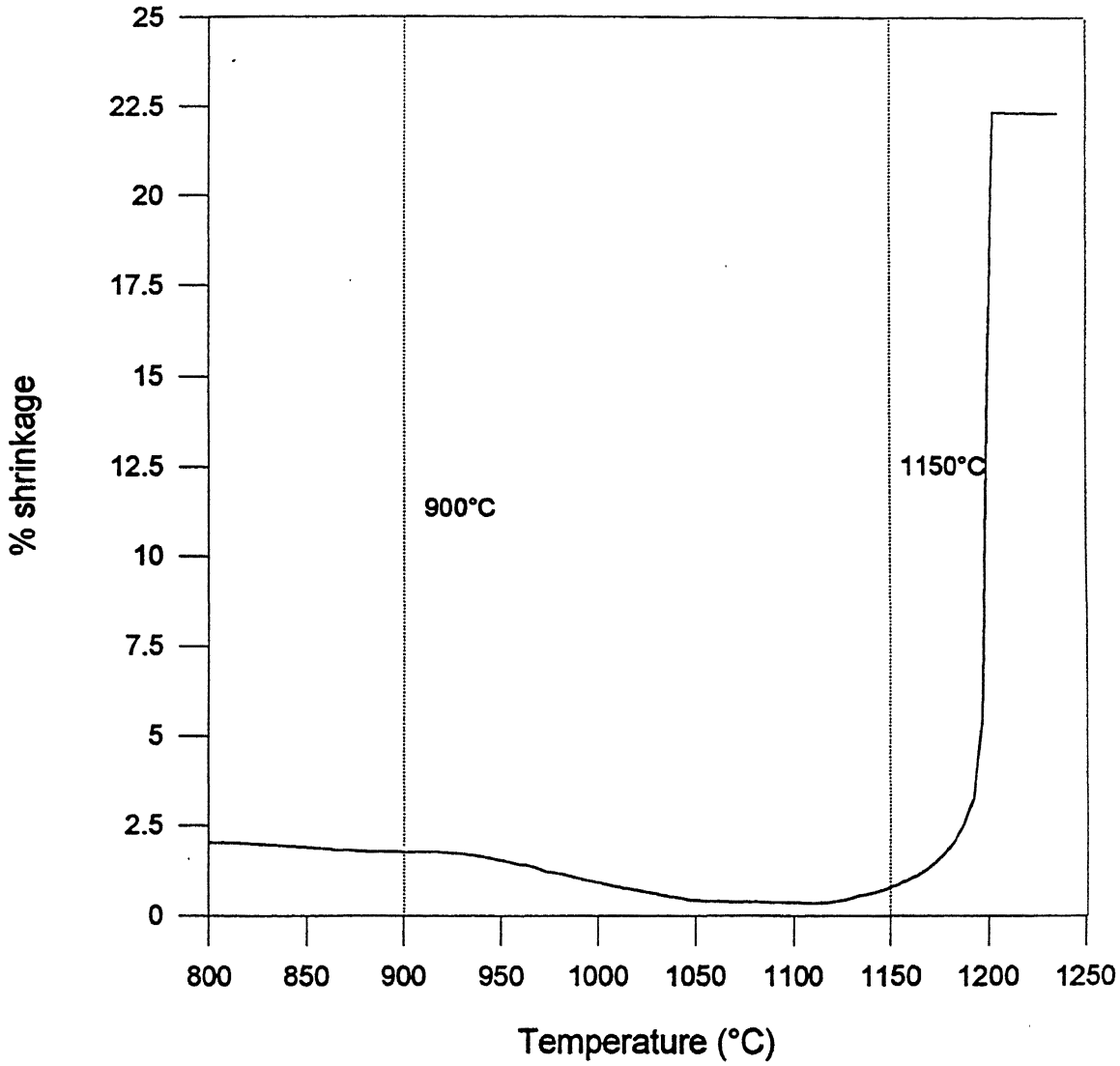

Figure 1.6(b) Dilation plot of KH-C50 showing swelling between 900 °C and 1150 °C associated with liquid phase formation [22].

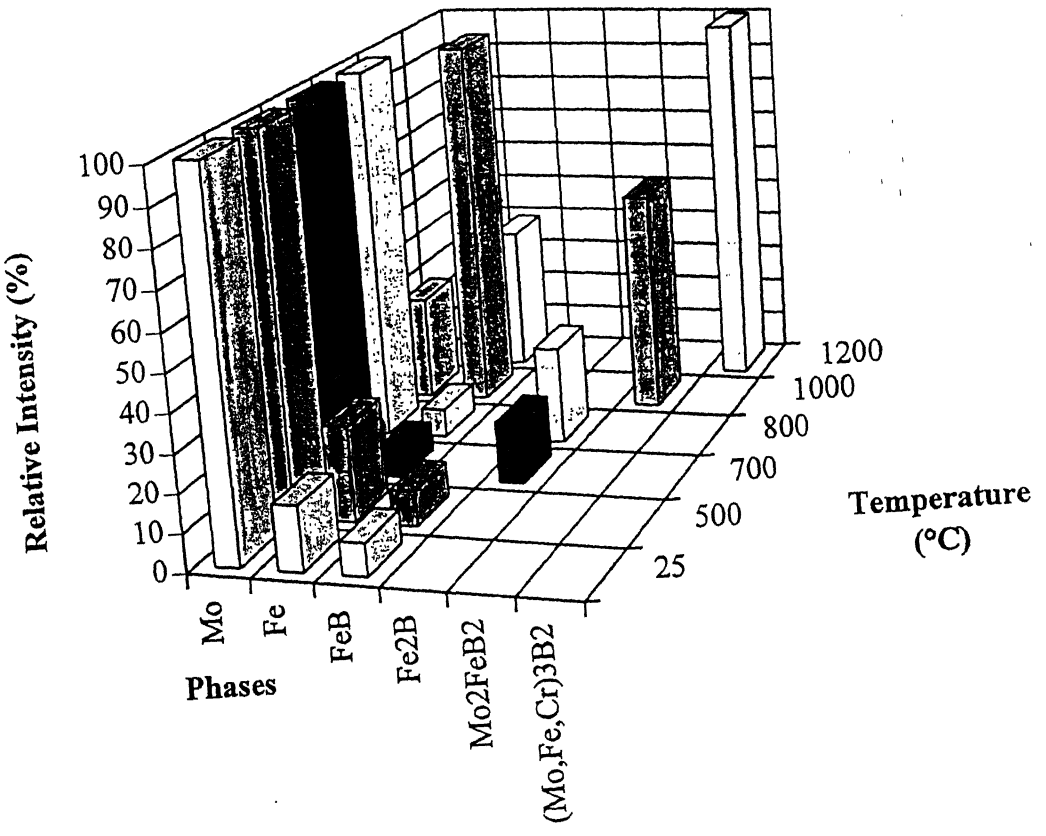

Figure 1.7 Relative measure of various phases present at a given sintering temperature [12]

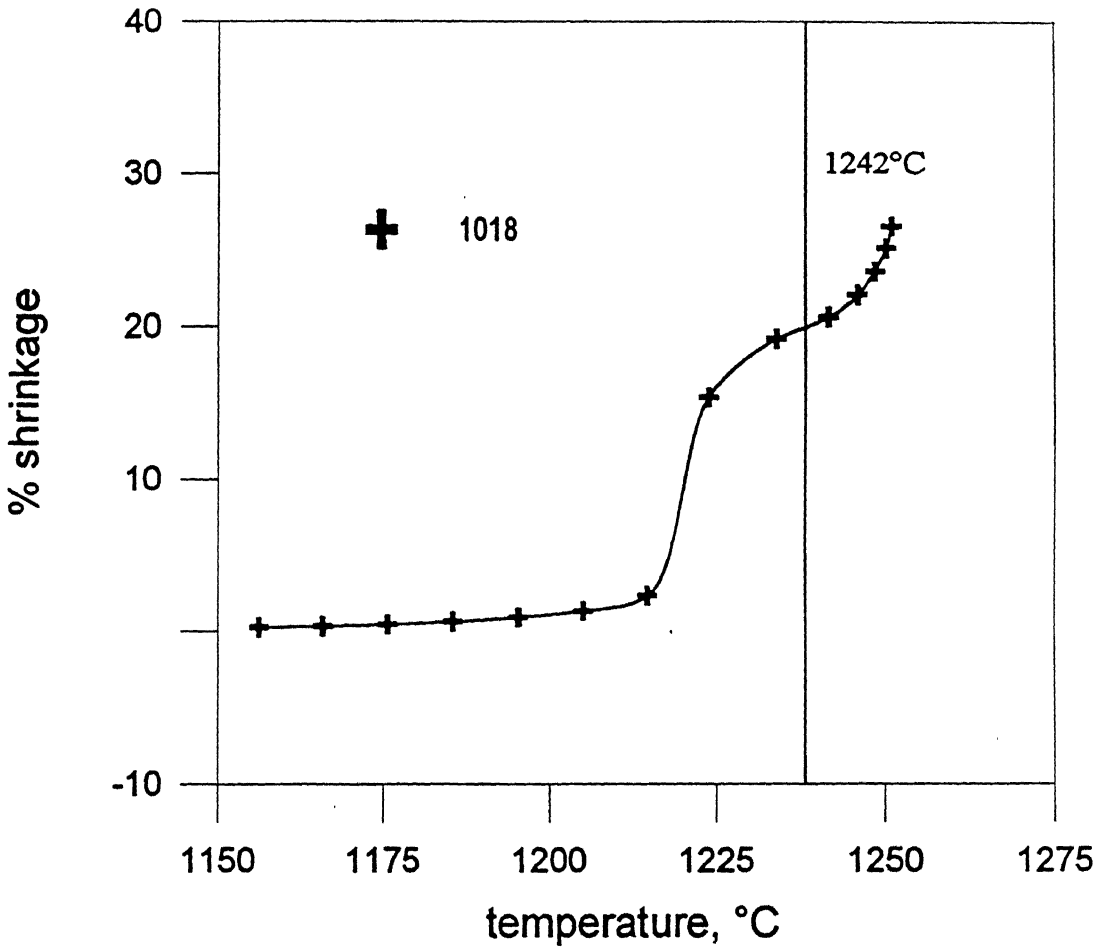

Figure 1.8 Dilation plot of KH-C50 sinter bonded onto 1018 steel substrate [22].

Chapter - 2

Experimental Procedure

2.1 Raw Materials

2.1.1 Green KH-C50 Sheets

The Mo_2FeB_2 based boride cermet material used in the present research had the designation KH-C50 and was obtained from Toyo Kohan Co. Ltd. Japan. It consisted of mixture of elemental powders of molybdenum, iron, chromium, nickel and a boride rich source FeB. The composition of the material is listed in Table 2.1.

The blend was available for research in the form of tape cast sheets of thickness 0.48 mm ± 0.02 mm and 1.06 mm ± 0.02 mm respectively. In the KH-C50 sheets of powders are bonded together by an organic binder. The organic binder used was Poly Vinyl Butyrl (PVB) based (about 50 volume %). The solvent used for tape cast sheets was ethyl alcohol. Prior to preparation of sheets, the powders were milled in acetone under a protective atmosphere of argon, then dried and granulated [3, 22]. The particle size distribution of the material as reported, is tabulated in Table 2.2.

2.1.2 Steel Plate

Low alloy steel plate of grade S-16, supplied by Taber Industries, New York was used for sinter bonding experiments. The company due to proprietary right did not disclose the exact composition of this steel. Thickness of this plate after surface finishing was 0.95 mm.

2.1.3 Silicon Carbide Fibers

Continuos SiC fibers manufactured by B. P. Metal Composites Ltd., England were used. The diameter of the fiber was in range of 101-102 μm. The theoretical density of the fiber is 3.17 g/cm^3 [20].

2.1.4 Aluminum Powder

Aluminum powder manufactured by Alcan Metal Powders, Elizabeth, New Jersy, USA was used. The specification of which is as under,

Grade	- MD –201
Purity	- 99.3 %
Apparent Density	- 1 g/cm^3.

2.1.5 Aluminum Bronze Powder

Aluminum Bronze powder supplied by Valimet inc., Stockton, California, USA. was used. The powder was atomized. Average particle size –100 mesh.

2.1.6 Copper Powder

Electrolytic copper powder supplied by Amrut Industrial Products, Mumbai was used. The chemical composition and powder characteristics are as follows,

Arsenic (As)	- 0.002 %,
Acid insoluble matter	- 0.05 %,
Heavy metals (Pb)	- 0.008 %,
Iron (Fe)	- 0.005 %,
Sulfide	- 0.005 %,
Copper	- Rest.

2.1.7 Poly Vinyl Alcohol (PVA)

PVA granules (cold processing) supplied by Burgoyne Burbidges and Co., Mumbai were used.

2.2 Sample Preparation Prior to Sintering

During few trial experimental runs of sinter bonding of boride based cermet onto steel, shrinkage behavior of cermet was observed. For obtaining final planner dimensions of cladded component of 70 X 15 mm, initial dimensions for steel and green KH-C50 sheets were calculated to be 94 X 16 mm. The steel plate was machined in the form of strips of dimension 94 X 16 mm using band saw. The green KH-C50 sheets were cut to above dimensions using a razor blade. The green KH-C50 sheets were either placed above the

steel strip or sandwiched between two steel strips without applying any interlamellar binder or compaction pressure.

In case of layered composites with or without Silicon carbide (SiC) fibers, the planner area of the green specimen was maintained 45 X 15 mm. SiC fibers were chopped to 45 mm length. The number of fibers in the composite was calculated on the basis of volume fraction calculation. Fibers were layered on to a green KH-C50 strip. Full care was taken to avoid overlapping and joining of these fine fibers with each other. Solution of PVA granules in water (10 wt %) was used as interlamellar binder, while placing second boride strip over to it. This was done in order to facilitate handling of green sandwiched composites.

In case of fibrous composites containing some interlamellar additives such as aluminum, copper or aluminum bronze powders, calculated amount (on the basis of volume fraction [18, 27]), was spread over the interface containing SiC fibers. Care was taken to ensure uniform distribution of this powder on to interlayer surfaces. Green compaction load of approximately 100 kPa was applied on lamellar compacts manually.

2.3 Debinding and Sintering

Debinding and sintering were carried out in laboratory type SiC-heated horizontal tubular furnace (Rating 1.5 kVA, 240 V, 10 A). The furnace tube

was made up of recrystallised alumina (inner diameter 38 mm, length 980 mm). In the present work, two sintering atmospheres namely vacuum and hydrogen were used. The system was capable of producing vacuum of the order of 0.1 mbar using ED-6, direct drive rotary vacuum pump (Hindhivac Ltd., Banglore; make). The furnace had a heating zone of approximately 105 mm in the temperature range of 1250 °C – 1350 °C with an accuracy of ± 3 °C.

In the present work two different sintering cycles were employed. The time – temperature plot of the cycles is shown in Fig. 2.1. The cycle 'A' has lower heating rates as compared to cycle 'B'. In cycle 'A' debinding carried out 400 °C for 30 minutes and then final sintering at 1245 °C for 30 minutes. On the other hand cycle 'B' has debinding stage at 400 °C which lasts for 60 minutes followed by a reduction stage at 1000 °C which lasts for 60 minutes and then final sintering at 1245 °C for 30 minutes. In both cycles cooling was done in prevailing atmosphere at an average rate of 2–3 °C / min.

For sintering samples were carried in a graphite boat into tube furnace. In order to minimize sticking of the samples with boat and to protect them from impurities, samples were puffed using hexagonal boron nitride powder. Steel – boride cermet layered samples were placed with steel strip at bottom and boride strip above it. No external loading on these samples was done. But in case of fibrous composites minor external pressure (~200 Pa) was held over

the samples to minimize their distortion during sintering. This external load was in the form of graphite plate.

2.4 Densification Behaviour

2.4.1 Linear and Volumetric Shrinkage

Linear dimensions of the sintered samples were measured using vernier calipers and screw gauge. As there may be uneven shrinkage in the samples, average of four measurements of each dimension is reported. The formulae used for calculations are as follows,

$$\delta l = \left(1 - \frac{ls}{\lg}\right) \times 100\%$$

$$\delta V = \left(1 - \frac{ls \times ws \times ts}{\lg \times wg \times tg}\right) \times 100\%$$

Where,

lg, wg, tg - length, width and thickness of green compact,

ls, ws, ts - length, width and shrinkage of sintered compact,

δl - % linear shrinkage in length,

δV - % volumetric shrinkage.

2.4.2 Total Sintered Porosity

Sintered density of the samples was measured using 'Archimedes Principle', where the partial loss of weight of the material immersed in water,

is a measure of volume of the material. For internal pore volume calculation, the xylene impregnation was done by placing the sample in xylene bath under vacuum. The sintered density was calculated by following relationship,

$$\rho_s = \frac{W_a}{W_{xa} - W_{xw}}$$

Where,

W_a - weight in air,
W_{xa} - weight after xylene impregnation in air,
W_{xw} - weight of the xylene impregnated sample immersed in water.

The total sintered porosity (ε_{ts}) is evaluated using following formula,

$$\varepsilon_{ts} = \left(1 - \frac{\rho_s}{\rho_{th}}\right) \times 100\%$$

Where,

ρ_{th} - theoretical sintered density of the samples (by Rule of Mixture),
ρ_s - Sintered density.

2.5 Mechanical Properties

The following mechanical properties were evaluated as described below.

2.5.1 Vickers Macrohardness

Vickers Macrohardness of the polished specimens were measured on Leco V-100-C1, Hardness Tester, manufactured by Akashi Corporation, Japan. The load of 10 kgf and indentation time of 15 seconds was maintained.

2.5.2 Vickers Microhardness

The microhardness of the samples was measured using Leitz Miniload Microhardness Tester (5g – 500g), manufactured by Leitz Wetzlar, Germany. The samples were finely polished using 0.3 μm alumina slurry, for accurate measurement. The indentor was a square base diamond pyramid with included angle 136°. For microhardness of boride cermet load of 500g and indenting time of 30 sec. was maintained. Vickers microhardness was calculated using following formula,

$$Hv = 1854.4 \times \frac{p}{d^2} \qquad kg/mm^2$$

Where,

p - indenting load, g;

d - average value of measurement of two diagonals of rhombohedral indention, μm.

2.5.2 Ultimate Tensile Strength

The ultimate Tensile Strength (UTS) of the samples of the cermet cladded steel samples, was done on Instron 1195 machine having load capacity range of 1 N – 100 kN. The load and extension data were automatically recorded on a plot. The formula used is as under,

UTS (M Pa) = Maximum load(N) / Cross-sectional load (mm^2)

Full-scale load of 10 kN, crosshead speed of 0.5 mm / min was used.

2.5.3 Transverse Rupture Strength

The Transverse rupture strength (TRS) of the layered boride cermet and its composites was performed on same Instron machine. The load and deflection data were automatically recorded on a plot. The formula used is as under [20],

$$T.R.S.(MPa) = \frac{1.5 \times p \times l}{w \times t^2}$$

Where,

p - fracture load, N;
l - span length, mm;
w - width of the test specimen, mm;
t - thickness of the test specimen, mm.

For all the measurements a full-scale load of 0.5 kN, crosshead speed of 0.1 mm / min, and span length of 23 mm was maintained.

2.6 Microstructural Studies

2.6.1 Optical Microscopy

The cladded cermet – steel sample were cut using a Leco cutoff saw. All the samples were mounted in cold setting epoxy molds facing their cross-section upwards. Mounted samples were first ground on a grinding wheel, followed by belt grinding on a 120 grit SiC endless belt. Sequential grinding was done on papers with decreasing roughness of 200, 320, 500, 1000 grit. The ground samples were then subsequently polished using 0.3 μm alumina slurry. Optical microscopic examination was done in as polished, and Nital etched condition. Nital used was 2 % HNO_3 solution in alcoholic base.

For observing boride grain morphology clearly, a boride coloring PPP reagent was also used. The composition of PPP reagent is as follows [3],

10g - $K_3[Fe(CN)_6]$,
1g - $K_4[Fe(CN)_6].3H_2O$,
30g - KOH,
100g - H_2O.

The action of this coloring reagent is slow, so either it is applied at elevated temperature of 60 °C or etched for few minutes.

2.6.2 Scanning Electron Microscopy

The fractured surfaces of the tensile and TRS tested samples were observed using JEOL, JSM – 840 A, scanning microscope. Operating voltage

was 10-15 kV and probe current ranged from 1 X 10^{-10} to 5 X 10^{-8}A in secondary electron imaging mode

2.6.3 Boride Grain Size Measurement

Boride grain size measurement was done on cermets sintered in either hydrogen or vacuum. It was done using measuring its size on graduated scale fitted in the eyepiece of the microscope. Proper calibrations were done for the magnifications of eyepiece and objective of the microscope. The average value of approximately 5-6 test lines, per sample, containing boride and binder intercepting grains was reported.

2.7 X-ray Diffraction Analysis

X-ray diffraction studies on the green and sintered of cermets were carried out on Rich Seifert & Co., Germany make, ISO Debyeflex – 2002 diffractometer . The various parameters during in the experiment are as given below,

Target (Radiation)	- Cu (K_α),
Wavelength, λ	- 1.541838 X 10^{-10} m,
Scanning speed	- 3°/ min, (in 2θ),
Chart speed	- 30 mm/min,
Counts / min	- 5000,
Time constant	- 10 s,
Amperage	- 20 mA,
Voltage	- 30 kV.

The inter-planner spacing (d_{hkl}) of various phases was calculated using Bragg's Law [28],

$$d_{h_i k_i l_i} = \frac{\lambda}{2\sin\theta_{h_i k_i l_i}} \mathring{A}$$

Where,
λ - wavelength of X-ray radiation used, Angsrom;
θ_{hkl} - Bragg angle of the (h k l) diffracting planes,degrees.

Indexing of X-ray diffraction patterns were carried out by matching using computer package of Joint Commission for Powder Diffraction Standard (JCPDS), ed. 1996.

2.8 Electron Probe Micro Analysis

The electron probe micro analysis of the diffusion zone of cermet – steel interface was carried out using JEOL, Superprobe, JXA – 8600 MX. The sample was finely polished as described in section 2.6.1. The probe current was in range of 2.3 – 2.9 X10^{-8} A. Analysis points were taken on a straight line across the diffusion zone.

Table 2.1 Material composition of 'as received' KH- C50.

Element	**Molybdenum**	**Iron**	**Chromium**	**Boron**	**Nickel**
Wt %	42.7	39.3	10.2	5	2.8

Table 2.2 The powder characteristics of the base material 'KH-C50' before green sheet formation.

Particle Size Distribution	
D_{10}	2.2 μm
D_{50}	6.3 μm
D_{90}	14.3 μm
Particle Shape	Irregular

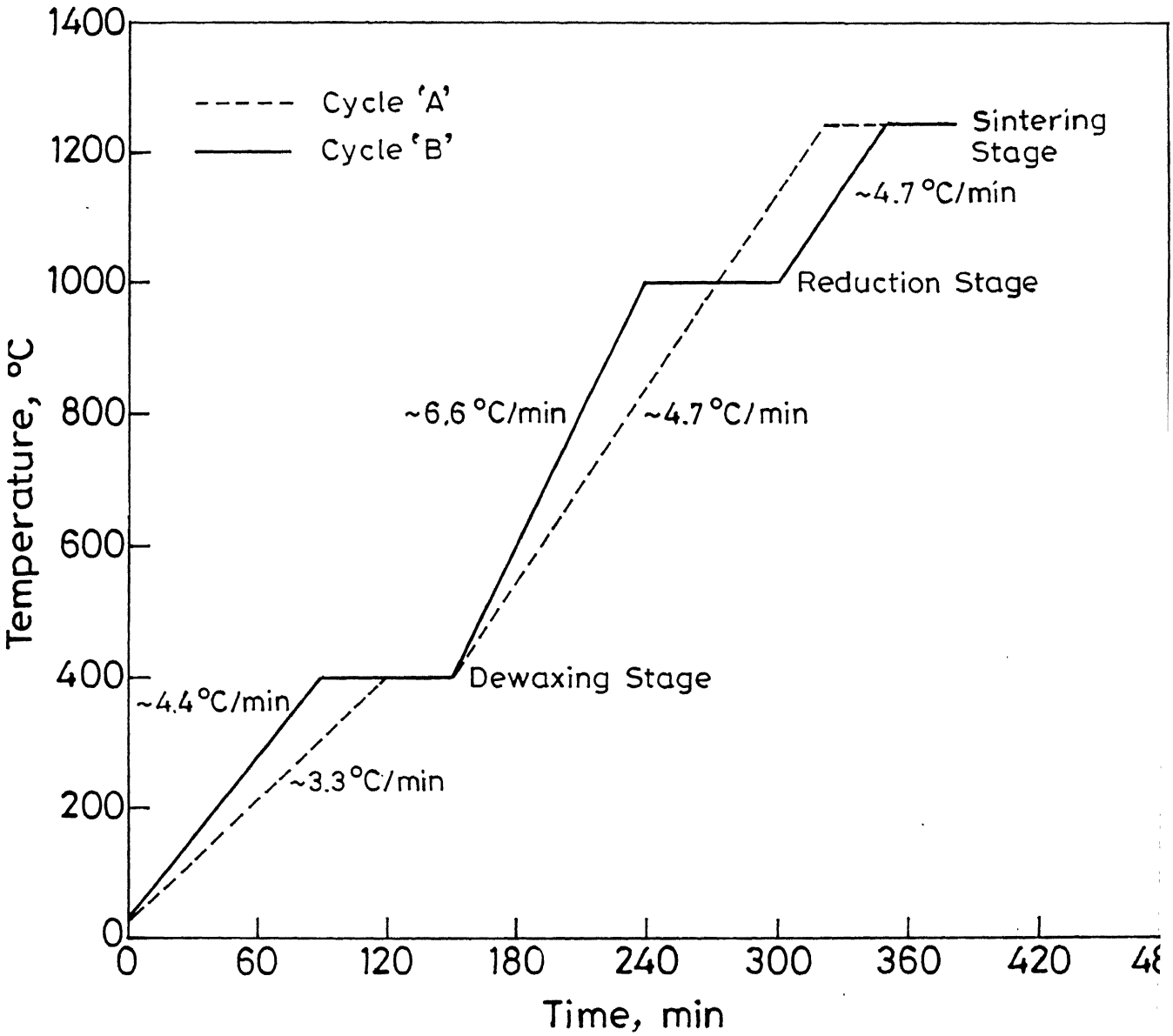

Figure 2.1 Time – temperature plot of sintering cycles 'A' and 'B'.

Chapter – 3

Experimental Results

The results of present investigation are divided into three sections. Section 3.1 deals with sintering parameters and properties of boride cermets. The results pertaining to investigation of sinter bonding of boride cermet with steel substrates is presented in Section 3.2. While the Section 3.3 enlists the results of experimental work done on processing / properties relations of layered composites of boride cermet with SiC fibers.

3.1 Sintering of Boride Cermet

3.1.1 Densification Behaviour

In the present investigation the boride based cermet (KH-C50) has been sintered in two atmospheres hydrogen and vacuum, according to two different heating cycles 'A' and 'B'. As it is evident from the Table 3.1 and 3.2 that hydrogen sintered layered cermets have remarkably higher porosity than those sintered in vacuum. The sintering cycle 'B' gave better densification than cycle 'A' in vacuum (Sample 1-2, Table 3.2), where as in hydrogen, cycle 'A' sintered samples have lower porosity (Sample 2 and 12; Table 3.1).

Application of PVA as interlamellar binder helped in attaining lower interfacial air entrapment and hence better bonding (Sample 1 and 2, Table 3.1). In triple layered compacts the sintered porosity was more than two layered compacts (Sample 2 and 3, Table 3.1).

3.1.2 Mechanical Properties

The variation of TRS of layered cermets, sintered in different atmosphere and cycles is remarkable. Vacuum sintered cermet (Sample 1 and 2, Table 3.2) have better TRS than hydrogen sintered cermet (Sample 2 and 12, Table 3.1). The samples sintered in vacuum according to cycle 'B' (Sample 2, Table 3.2) has better mechanical properties than those sintered according to cycle 'A'. Whereas in hydrogen, samples sintered according to cycle 'A' (Sample 2, Table 3.1) gave better properties.

A comparative view of various mechanical properties of the hydrogen cycle 'A' sintered and vacuum cycle 'B' sintered cermets is shown in Fig. 3.1 for comparison. The variations in TRS, macrohardness and microhardness are shown in the bar chart form in the same figure. The properties of the cermet are varying primarily according to porosity, shown in the same Fig. 3.1.

3.1.3 X-ray Diffraction Analysis

X-ray diffraction analysis has been done to conclusively establish the phases present in the material. Fig. 3.2 has two parts, part (a) is the XRD of

'as received' green form of cermet (KH-C50), while part (b) is the XRD pattern of sintered boride cermet.

Fig. 3.2 (a) shows the molybdenum and iron in their elemental state and FeB in the compound state. The peaks of chromium and nickel are not prominent due to their rather low amounts.

Fig. 3.2 (b) shows that in sintered state almost all peaks establish the formation of ternary boride Mo_2FeB_2. Chromium forms solid solution with ternary boride, resulting $(Mo, Fe, Cr)_3B_2$. Presence of this solid solution is confirmed by earlier investigation [12].

3.1.4 Optical Microscopy and SEM Fractography

Optical micrographs show a finely dispersed ternary boride phase Mo_2FeB_2 in an iron-based matrix. Fig. 3.3 (a)-(c) show the micrographs of the vacuum sintered samples according to cycle 'B' (Sample 2, Table 3.2) in three different conditions. Fig. 3.3 (a) is in 'as polished' condition. In this micrograph even though the ternary boride grains are visible, but their morphology is not clear. Individual grains and coalesced grains can not be distinguished. Fig. 3.3 (b) corresponds a Nital etched one, where the etching agent attacks the iron based binding matrix of the cermet leaving the boride phase unattacked. Fig. 3.3(c) shows the same specimen being etched with a boride-coloring reagent called PPP. It reacts with boride grains leaving them

darker in the micrograph. The iron based binding matrix remains white. PPP makes the boride grain morphology study convenient.

Fig. 3.4 comprises of the micrographs of hydrogen sintered cermet with and without PVA binder at interface, in the green state. Fig. 3.4 (a) shows the interface of the sample without PVA binder (Sample 1, Table 3.1), the wider interfacial gap exhibit poor interlayer bonding. On the other hand Fig. 3.4 (b) shows a rare and thin interlamellar gap in the sintered sample with interlayer PVA binder (Sample 2, Table 3.1) confirming that PVA helps in attaining better interlayer bonding.

The SEM fractographs (Fig. 3.5(a) and (b)) show brittle fracture mode of hydrogen sintered cremet after TRS testing.. Dispersed rounded pores are visible in the hydrogen cycle 'B' sintered cermet sample. Presence of large number of pores weakens the material. On the other hand, Fig. 3.5 (c) and (d) are the magnified view of fractured surfaces of vacuum sintered samples.

3.1.5 Grain Size Measurement

The average grain size of finely dispersed ternary boride phase was found to less than 3 μm. There is insignificant variation of grain size in samples sintered in either of atmospheres or cycles.

3.2 Sinter bonding of Boride Cermet onto Steel Substrates

The sinter bonding of boride cermet (KH-C50) onto steel substrates proceeds through eutectic liquid phase of iron and boron at the interface. All the reported sinter bonding experiments in the present investigation, described in following sections, have been carried out in hydrogen according to cycle 'A'.

3.2.1 Densification Behaviour

3.2.1.1 Total Sintered Porosity

From Table 3.3 it is clear that boride cermet lamella get sintered well when sinter bonded onto steel substrates. In case of steel plate cladded with boride cermet layer (Sample 1, Table 3.3), no air entrapment at the interface was observed and the cermet is almost fully dense. But the samples having sandwiched boride cermet layer (Sample 2 and 3, Table 3.3), have increased total sintered porosity. The entrapped air is in the form of big pores visible by naked eyes at the fractured cross-section.

3.2.1.2 Dimensional Changes

Table 3.3 reports the linear shrinkage of boride cermet layer sinter bonded onto steel. The percentage shrinkage in length, width and thickness has been denoted by l, w and t respectively. The cladded boride cermet layer on to

steel (Sample 1, Table 3.3) experiences shrinkage in all the dimensions, while in case of the samples having sandwiched boride cermet layer (Samples 2 and 3, Table 3.1) almost all of its shrinkage is in thickness dimension.

3.2.2 Ultimate Tensile Strength

Boride cermets are of very brittle nature. When steel is cladded with boride cermet, its tensile strength gets adversely affected. Fig. 3.6 illustrates the variation in tensile strength of cermet cladded steel. Higher is the volume fraction of the cermet cladding, lower is the tensile strength of the part.

To have picture of state and strength of the uncladded steel undergoing similar heating cycle, the steel was heated in similar fashion as that of sinter bonding. The variation in tensile strength, percentage elongation and microhardness after heating and in 'as received' state are shown in Fig. 3.7.

3.2.2 Microhardness

Fig. 3.8 illustrates the variation in microhardness of the boride cermet near to the cermet-steel diffusion zone. It shows an increase in microhardness from cermet-steel interface to the dip within cermet region. It shows that interface zone is of few tens of micrometers, after which the cermet attains its full hardness.

3.2.3 EPMA of Cermet – Steel Diffusion Zone

The boride cermet cladded steel sample (Sample1, Table 3.3) has been investigated by Electron Probe Micro Analyser (EPMA). Fig. 3.9 shows the variation of different constituent elements namely molybdenum, iron, chromium and nickel of the boride cermet and steel. Molybdenum and iron seems to be having major role across the diffusion zone. Chromium and nickel are fairly constant up to the interface across which their presence vanishes sharply.

3.2.4 Optical Microstructures and SEM Fractographs

The optical microstructure of the cermet cladded steel sample (Sample 1, Table 3.3) is shown in Fig. 3.10. The interface between boride cermet and steel is clearly visible. There is presence of fine eutectic at the interface. The interfacial region consists of solidified liquid extending from the eutectic to the densified boride cermet. Fig.3.10 (a) shows the magnified view of boride region. The boride cermet is almost fully dense with homogenous distribution of ternary boride in the iron-based matrix. Few of the boride grains are coalesced. Fig. 3.10 (c) shows the ferritic microstructure in the steel substrates.

The SEM fractograph of the tensile tested cermet cladded steel sample is shown in Fig. 3.11, where the three layers namely boride cermet cladding, diffusion zone and the steel substrates are visible. Fig. 3.8 (a) is magnified

view of the boride cermet cladding which shows a relatively brittle fracture. On the other hand Fig. 3.11 (c) shows the ductile nature of the steel base. Fig. 3.11 (b) shows the intermediate picture. There is directionally grown microstructure.

In the case of samples having sandwiched boride cermert layer (Sample 2 and 3, Table 3.3) between the two steel plates some interesting microstructural features are evident. Fig. 3.12 shows the optical microstructure of the cross-section of these samples etched with Nital. Fig. 3.12 (a) shows the dendritic grain growth of the iron-based matrix of the cermet (the white phase), while the ternary boride phase seems to be lumped together as darker phase in the micrograph. Fig. 3.12 (c) shows the section of thinner boride layer containing sample (Sample 3, Table 3.3) where the dendrite formation is more prominent. Fig. 3.12 (b) and (d) show the magnified views of thicker and thinner boride layers respectively.

Fig. 3.13 is the SEM fractograph of the tensile tested sample with sandwiched boride layer between two steel plates (Sample 2, Table 3.3). The Fig. 3.13 (a) shows brittle fracture of boride cermet layer, where the directionally grown microstructure is visible. While Fig. 3.13 (b) shows relatively ductile cellular type microstructure in case of cermet / steel diffusion layer.

3.3 Layered Composites of Boride Based Cermet With SiC Fibers

3.3.1 Densification Behaviour

Table 3.1 enlists the composites sintered in hydrogen while Table 3.2 tabulates the results pertaining to the composites sintered in vacuum.

3.3.1.1 Total Sintered Porosity

The amount of retained porosity in composites found to depend largely on the sintering environment used. Fig. 3.14 shows the variation of percentage porosity in layered composite with sintering atmosphere, heating cycle and volume percent of SiC fibers in the composites. It is noteworthy that total porosity decreases drastically when sintering atmosphere is changed from hydrogen to vacuum. High residual porosity in composites sintered in hydrogen is mainly contributed by entrapped gases at the interface. This air entrapment is in the form of big pores, which badly affects the sample geometry. Samples hydrogen sintered according to cycle 'B' has very poor densification, where as after vacuum sintering for the cycle good densification is observed. Triple layered composites have more percentage porosity than two layered ones with same volume percent of SiC fibers (Samples 6, 10, Table 3.1). The presence of interlayer metallic additives adversely affects the densification (Sample 7-9, Table 3.1).

3.3.1.2 Dimensional Changes

Dimensional changes occurring in the composites along length, width and thickness are reported in the Table 3.1 and 3.2. The volumetric shrinkage is the direct indicator of densification. The linear shrinkage of the composite shows some anisotropic behaviour. Fig. 3.15 reports the shrinkage occurring in the fiber laying direction of the composite. As the fibers are introduced between the boride layers, their lengthwise shrinkage drops drastically. As the volume percent of SiC fibers is increased, lengthwise shrinkage drops further, irrespective of the sintering atmosphere and cycle.

3.3.2 Transverse Rupture Strength

In case of inherent brittle materials like boride based fibrous composites, the Transverse Rupture Strength (TRS) is meaningful parameter to be investigated.

The TRS data of the composites is tabulated in Table 3.1 and 3.2. Fig. 3.16 shows the comparative view of TRS variation with different sintering cycles. It is noteworthy that residual porosity dictates the TRS of the composite. The vacuum sintered samples have remarkably higher TRS than those sintered in hydrogen for the same volume percent of SiC fibers. Introduction of SiC fibers between the boride cermet lamellae makes the TRS to fall. The vacuum sintered sample as per cycle 'A' is an exception to the

above statement. On increasing the fiber volume fraction in the composite, the TRS invariably falls.

In order to improve wetting between SiC fibers and the boride based cermet lamellae some interlayer metallic additives were incorporated. The effect of these additives on TRS of 2 vol. % SiC containing composites is tabulated in Table 3.1(Sample 7-9). Aluminium powder was found to be highly damaging to the interlamellar bonding. Composites produced were too fragile (Sample 7, Table 3.1). Aluminium – bronze gave better results than pure aluminum (Sample 8, Table 3.1). Copper a was also tried(Sample 9, Table 3.1), it gave better results than even aluminium – bronze. However interlayer additives used weaken the bonding and no useful purpose is achieved.

3.3.3 Microhardness

Fig. 3.17 is showing the comparative view of microhardness variation in straight boride cermet (Sample 1, Table 3.2) and 2 % SiC, composite (Sample 3, Table 3.2) sintered in same fashion. In case of straight boride cermet sample the interface was selected on the microscopic measurement at rather lower magnification, while in the case of lamellar composite interface was clearly visible. As one traverses from the interface there is some increase in microhardness followed by a fall. This trend is followed in both the cases.

3.3.4 Optical Microstructures and SEM Fractography

The SiC fibers hinder the bonding of cermet lamellae. Fig. 3.18 (a) and (b) show the optical microstructures of hydrogen sintered composites (Sample 5 and 6, Table 3.1) with 2 and 4.4 vol. % SiC fibers. The black rounded fiber cross-sections are visible in the magnified view in Fig. 3.18 (a), while the Fig. 3.18 (b) is the micrograph showing the voids created at the interface. The randomly distributed rounded pores (darker) are also visible. Fig. 3.18 (c) and (d) are the micrographs of interface of vacuum sintered composites with 2 and 4.4 vol. % SiC fibers respectively (Samples 3 and 4, Table 3.2). Decrease in the percentage porosity as compared to hydrogen sintered ones is clearly visible in the micrographs. On comparing Fig. 3.18 (c) and (d) the increased irregularity at the interface with rise in volume percent of SiC fibers is evident.

Fig. 3.19 (a) and (b) are the fractographs of interfacial regions of hydrogen sintered composites (Sample 13 and 14, Table 3.1) with 2 and 4.4 vol. % SiC fibers respectively. The interlamellar void is clearly visible. Fig. 3.19 (c) and (d) are the fractographs of vacuum sintered composites (Sample 5 and 6, Table 3.2) with 2 and 4.4 vol. % SiC fibers respectively. Fig. 3.20 (a) and (b) are the fractographs of 2 vol. % SiC fiber composites the effect of interlayer aluminium-bronze additive at the interface containing SiC fibers. Fig. 3.20 (a) is the fractograph of the sample without any interlayer additive

(Sample 6, Table 3.1). The interfacial void is clearly visible as straight dark band across the micrograph, while SiC fibers can be seen as dark rounded series, below the interfacial band. While in Fig. 3.20 (b) shows the non-wetting nature of interlayer metallic additive aluminium-bronze (light colored lumps) with boride based cermet. The cermet lamellae have poor bonding hence wider interfacial gap. The SiC fiber can be seen in unbounded condition at the interface.

(Sample 6, Table 3.1). The interfacial void is clearly visible as straight dark band across the micrograph, while SiC fibers can be seen as dark rounded series, below the interfacial band. While in Fig. 3.20 (b) shows the non-wetting nature of interlayer metallic additive aluminium-bronze (light colored lumps) with boride based cermet. The cermet lamellae have poor bonding hence wider interfacial gap. The SiC fiber can be seen in unbounded condition at the interface.

Table 3.1 Results of hydrogen sintered layered boride cermet composites with or without SiC fibers.

S. No.	Sample	Schematic View	P.V.A. between lamellae during compaction	External pressure while sintering	Linear shrinkage* %	Volumetric shrinkage %	% Porosity	T.R.S. MPa	Remarks
				CYCLE 'A'					
1	Two ternary boride lamellae without fibers, without binder at interface.		No	No	l-32.4 w-31.8 t-14.4	60.5	25.0	371.6	Some air entrapment, poor bonding.
2	Two ternary boride lamellae without fibers, with binder at interface		Yes	No	l-30.4 w-31.6 t-24.0	63.8	16.7	378	Fewer air entrapment as compared to sample 1.better bonding.
3	Three ternary boride lamellae without fibers, with binder		Yes	Yes	l-17.5 w-35.5 t-25.3	60.0	20.3	222.5	reasonably good bonding.
4	4.4 vol. % SiC fibers sandwiched between ternary boride lamellae, without external load.		Yes	No	-	-	-	-	Gross distortion.
5	4.4 vol. % SiC fibers sandwiched between ternary boride lamellae, with external load.		Yes	Yes	l- 6.7 w-34.0 t-14.3	49.1	25.1	218.75	Poor bonding, better strength than that of sample 4.

2 vol. % SiC fibers sandwiched between ternary boride lamellae		Yes	Yes	l-11.1 w-30.1 t-33.6	59.0	28.1	264.4	Bonding is adversely affected by presence of fibers.
2 vol. % SiC fibers sandwiched between ternary boride lamellae with 2 vol % aluminium as additive at interface		Yes	Yes	-	-	47.0	-	Too fragile.
2 vol.% SiC fibers sandwiched between ternary boride lamellae with 2 vol. % aluminium-bronze as additive at interface		Yes	Yes	l-10.0 w-16.3 t-6.6	30.4	36.0	32.4	Better bonding as compared to sample 7. Poor strength.
2 vol. % SiC fibers sandwiched between ternary boride lamellae with 2 vol. % copper as additive at interface		Yes	Yes	l-18.6 w-34.6 t-33.3	64.3	21.8	127.1	Still strength is poorer than sample 6, however better than sample 7 or 8.
2 vol. % SiC fibers sandwiched between three ternary boride lamellae		Yes	Yes	l-11.1 w-41.4 t-62.6	15.1	51.3	194.4	Bonding is poorer than that of sample 6.
25 vol. % SiC fibers sandwiched between three ternary boride lamellae		Yes	No	-	-	-	-	Highly distorted, no bonding at all.

CYCLE 'B'

2	Two ternary boride lamellae without fibers, with binder at interface		Yes	Yes	l-25.2 w-33.9 t-5.3	53.0	37.0	294.8	severe air entrapment.
3	2 vol.% SiC fibers sandwiched between ternary boride lamellae		Yes	Yes	l-12.4 w-28.9 t-13.1	46.0	38.0	117.1	no air entrapment, but fragile , poor bonding.
4	4.4 vol. % SiC fibers sandwiched between ternary boride lamellae.		Yes	Yes	l-9.9 w -26 t-11.8	45.1	40.0	108	no air entrapment, but fragile , poor bonding.

Table 3.2 Results of vacuum sintered layered boride cermet composites with or without SiC fibers.

S. No.	Sample	Schematic View	Linear shrinkage* %	Volumetric shrinkage %	% Porosity	T.R.S. MPa	Remarks
1	Ternary boride lamellae, without fibers, sintered in vacuum cycle 'A'.		l - 20.0 w - 32.6 t - 34.9	64.9	2.0	421.6	distortion, no air entrapment.
2	Ternary boride lamellae, without fibers, sintered in vacuum cycle 'B'.		l - 25.0 w - 27.1 t - 39.8	68.1	0.3	636.1	lesser distortion than 1,no air entrapment.
3	2 vol. % SiC fibers sandwiched between ternary boride lamellae, sintered in vacuum cycle 'A'.		l - 17.8 w - 27.2 t - 44.0	66.5	3.1	645.7	moderate distortion, no air entrapment.
4	4.4 vol. % SiC fibers sandwiched between ternary boride lamellae, sintered in vacuum cycle 'A'.		l - 9.9 w - 32.2 t - 48.6	68.6	2.2	596.6	moderate distortion, no air entrapment.
5	2 vol. % SiC fibers sandwiched between ternary boride lamellae, sintered in vacuum cycle 'B'.		l - 14.7 w - 33.0 t - 48.6	64.8	3.8	416.4	lesser distortion than 3 and 4,no air entrapment.
6	4.4 vol. % SiC fibers sandwiched between ternary boride lamellae, sintered in vacuum cycle 'B'.		l - 10.2 w -34.8 t - 34.4	61.6	3.7	303.3	lesser distortion than 3 and 4,no air entrapment.

* l- lengthwise, w- widthwise, t- thicknesswise

Table 3.3 Results of sinter bonded boride cermet layer onto steel substrates

S.No.	Sample	Schematic View	Volume fraction of cermet layer % [Wt %]	Linear shrinkage of cermet layer* %	Volumetric shrinkage of cermet layer %	% Porosity in Sample	U.T.S. MPa	Remarks.
1	Steel cladded with ternary boride cermet layer.		37.5 [39.4]	l - 25.0 w - 6.7 t - 45.0	61.2	3.0	186	No air entrapment, excellent bonding.
2	Thicker ternary boride cermet layer sandwiched between two steel plates.		17.2 [18.5]	l ~ 0 w ~ 0 t - 63.4	63.4	4.9	280.7	Few air entrapment, excellent bonding.
3	Thinner ternary boride cermet layer sandwiched between two steel plates.		8.7 [9.5]	l ~ 0 w ~ 0 t - 60.0	60.0	6.5	325	few air entrapment, good bonding.

* l- lengthwise, w- widthwise, t- thicknesswise,

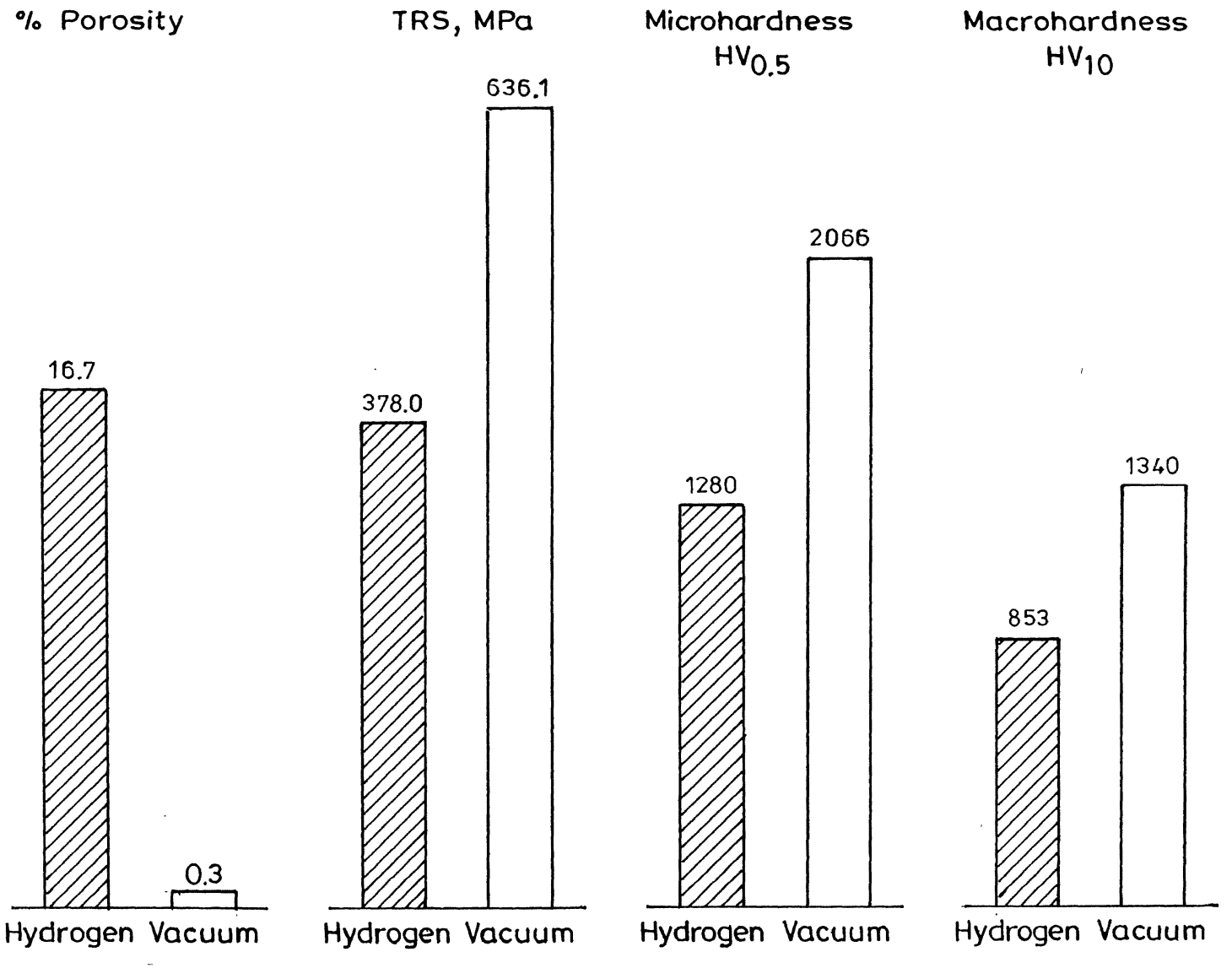

Figure 3.1 Properties of hydrogen and vacuum sintered boride cermet.

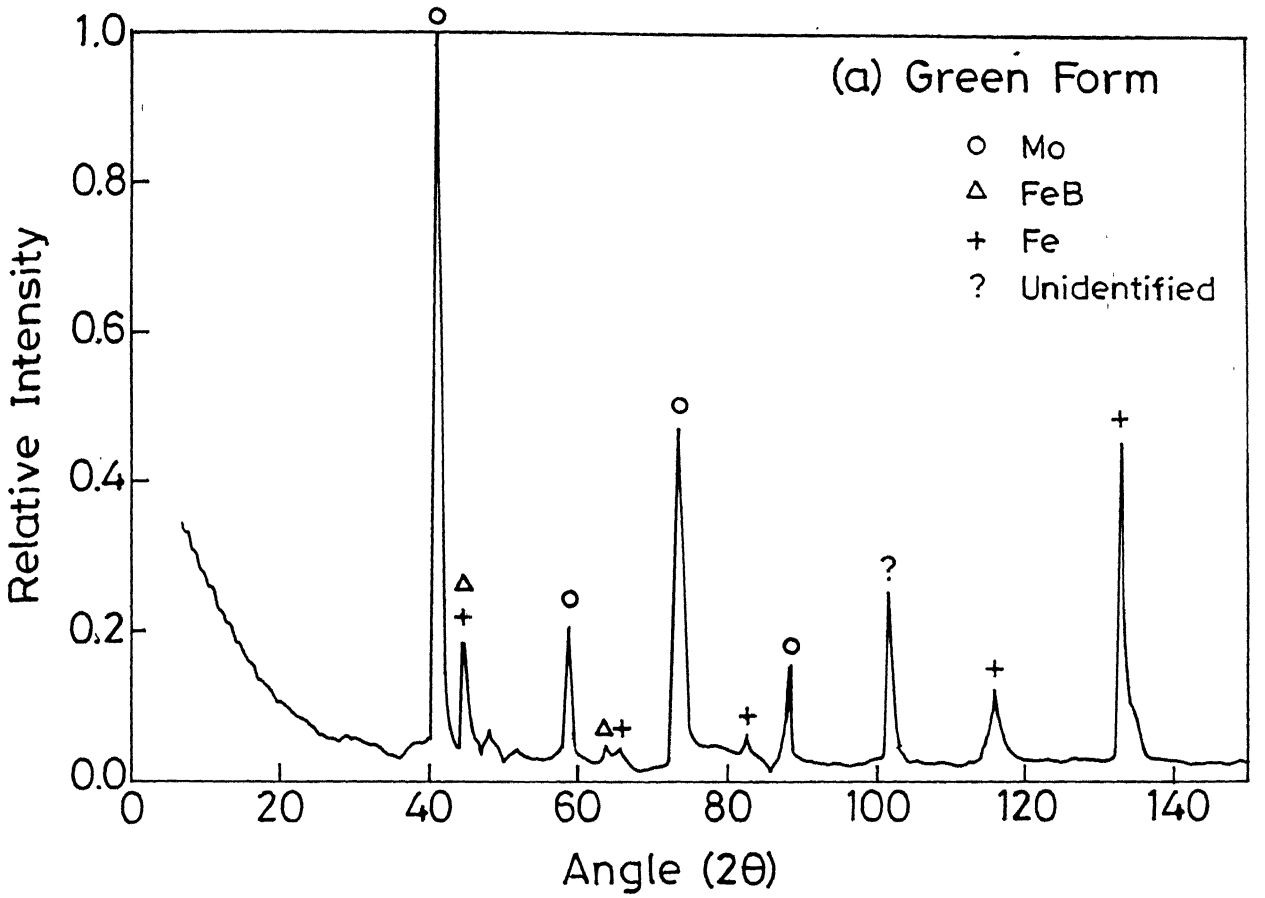
(a) Green Form
Mo
FeB
Fe
Unidentified
Relative Intensity
Angle (2θ)
1.0
0.8
0.6
0.4
0.2
0.0
0
20
40
60
80
100
120
140

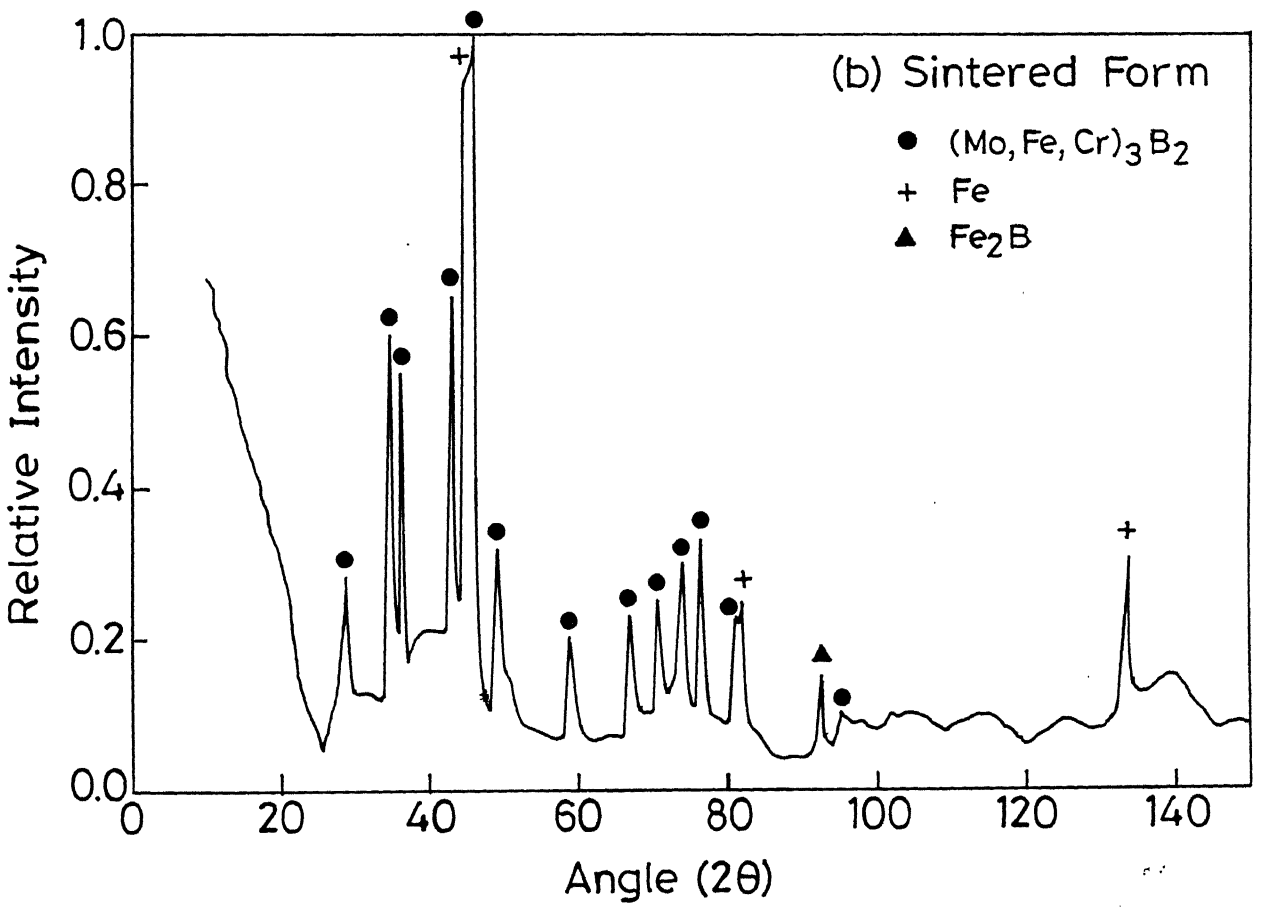
(b) Sintered Form
(Mo, Fe, Cr)3B2
Fe
Fe2B
Relative Intensity
Angle (2θ)
1.0
0.8
0.6
0.4
0.2
0.0
0
20
40
60
80
100
120
140

a

b

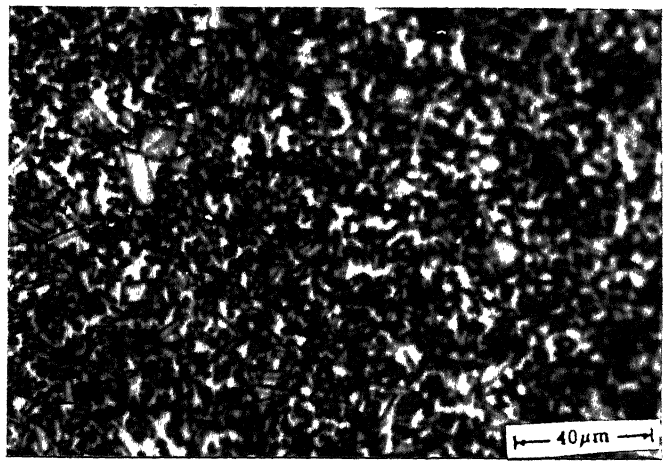

c

Figure 3.3 Optical micrographs of vacuum sintered boride cermet etched in different etching media (Samlpe 2, Table 3.2).

(a) as polished condition,

(b) etched with Nital

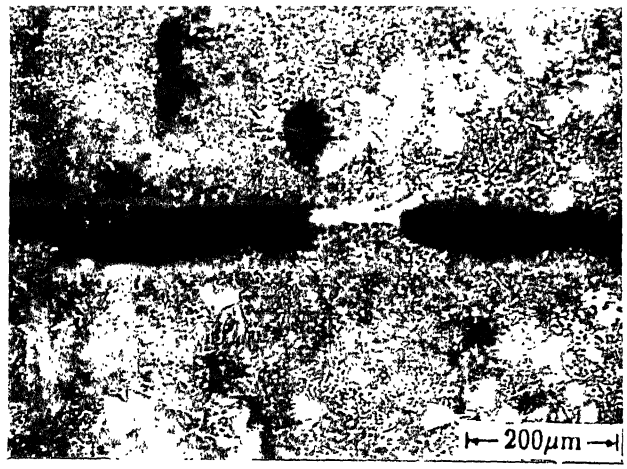

a

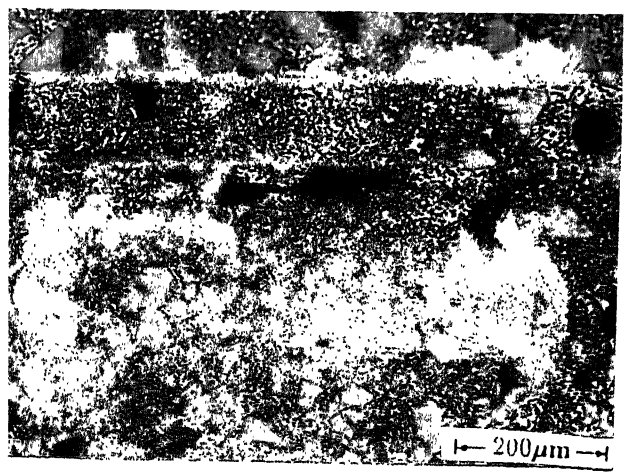

b

Figure 3.4 Optical micrographs of interface of hydrogen cycle 'A' sintered boride cermet.

(a) without PVA binder (Sample 1, Table 3.1)
(b) with PVA binder at interface during green compaction (Sample 2, Table 3.1).

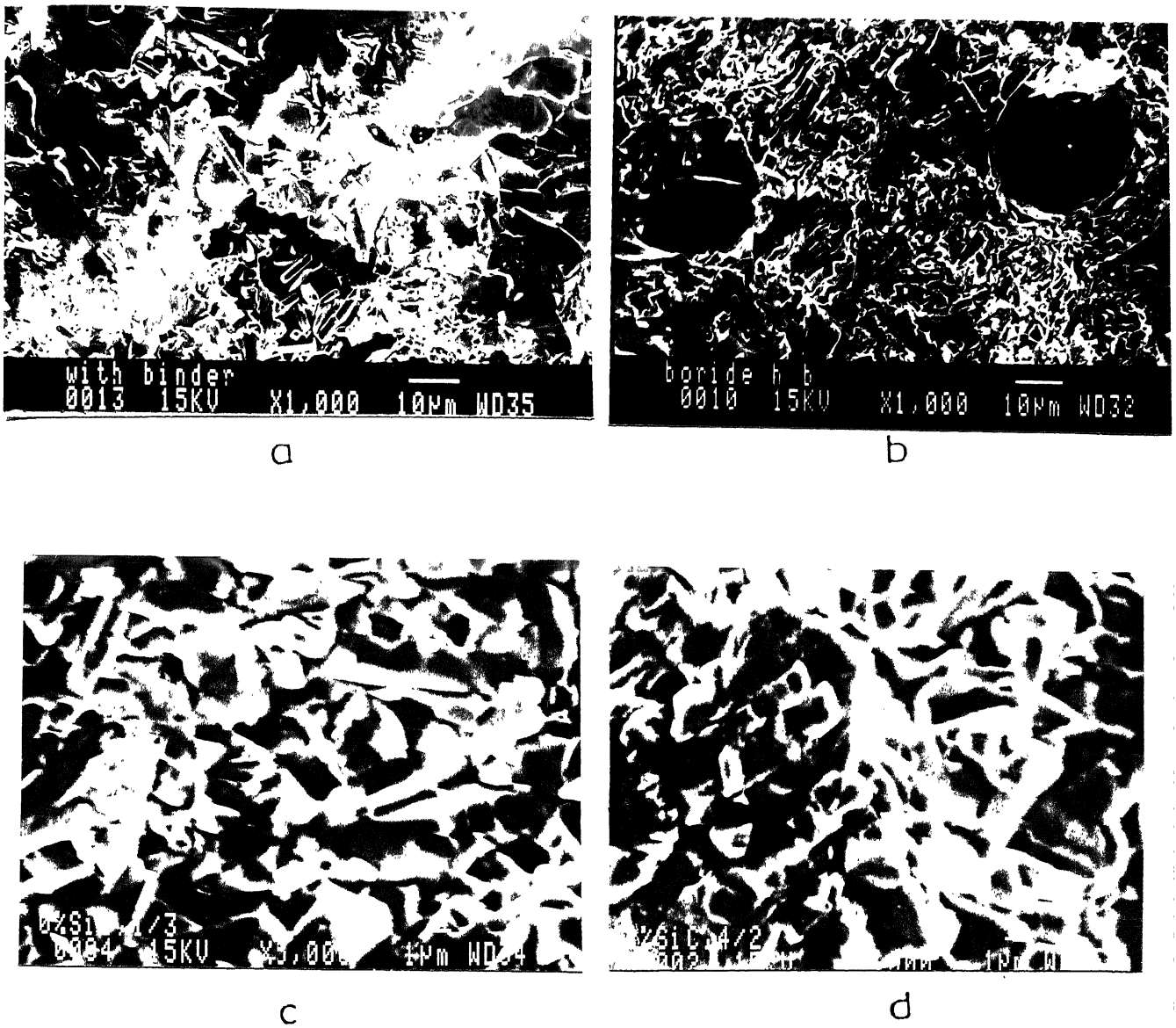

Figure 3.5 SEM fractographs of boride cermet samples after TRS test.
(a) hydrogen cycle 'A' sintered (Sample 2, Table 3.1),
(b) hydrogen cycle 'B' sintered (Sample 12, Table 3.1),
(c) vacuum cycle 'A' sintered (Sample 1, Table 3.2),
(d) vacuum Cycle 'B' sintered (Sample 2, Table 3.2).

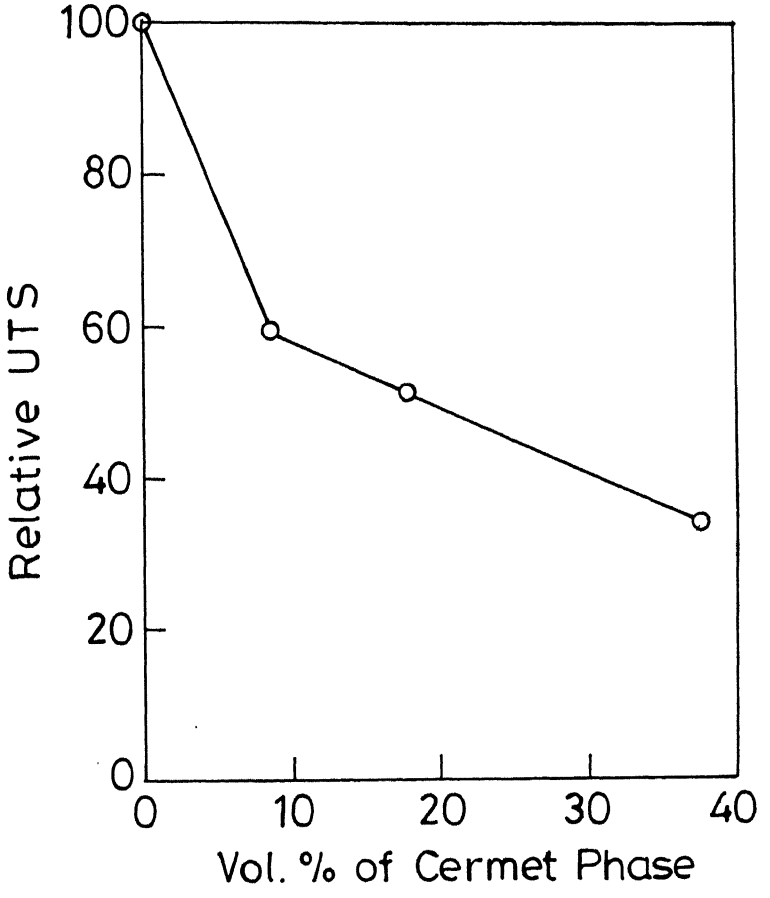

Figure 3.6 Variation of UTS of boride cermet cladded steel with volume percent of cermet phase.

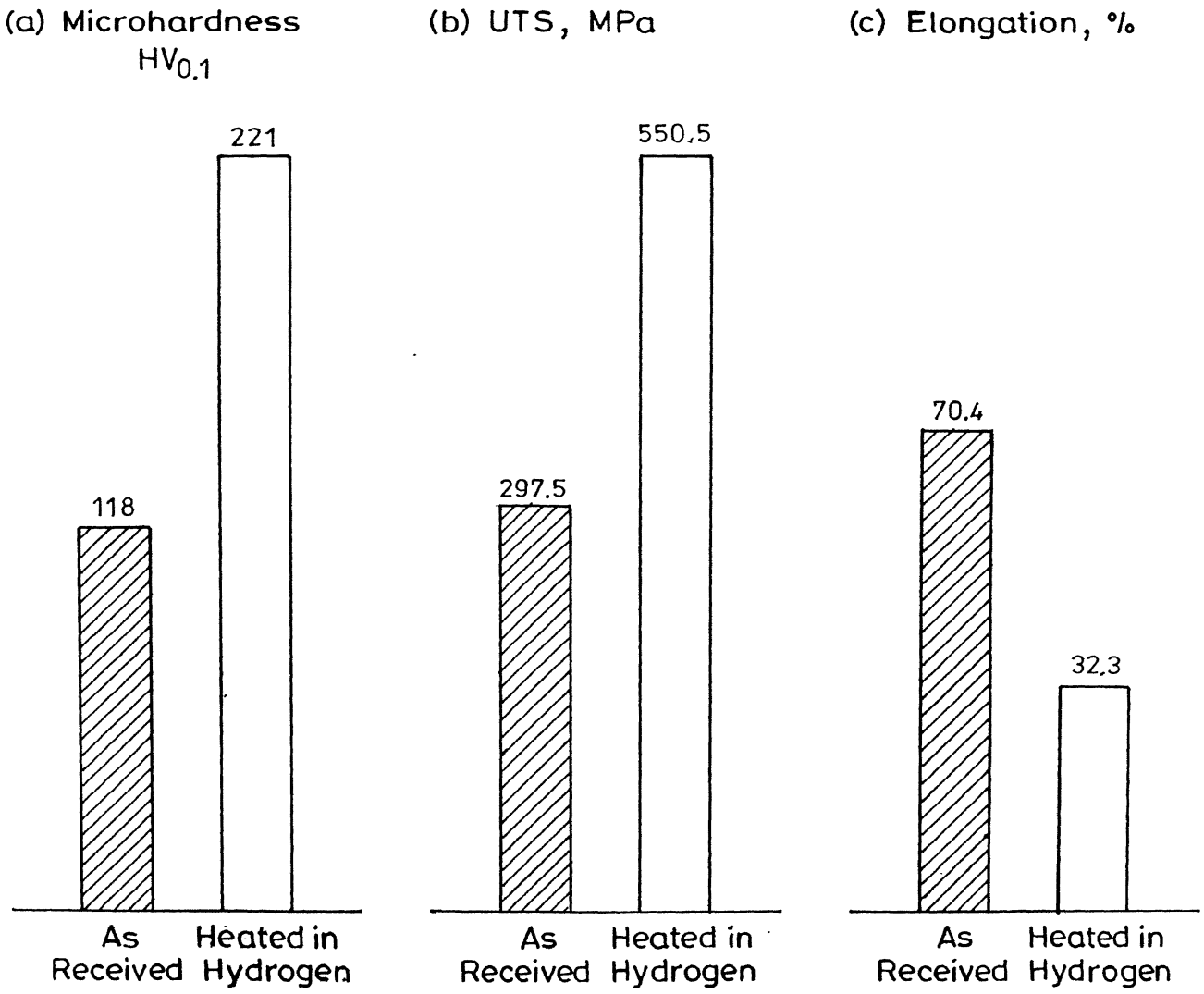

Figure 3.7 Variation in the mechanical properties of steel plate used as substrate (after heating).

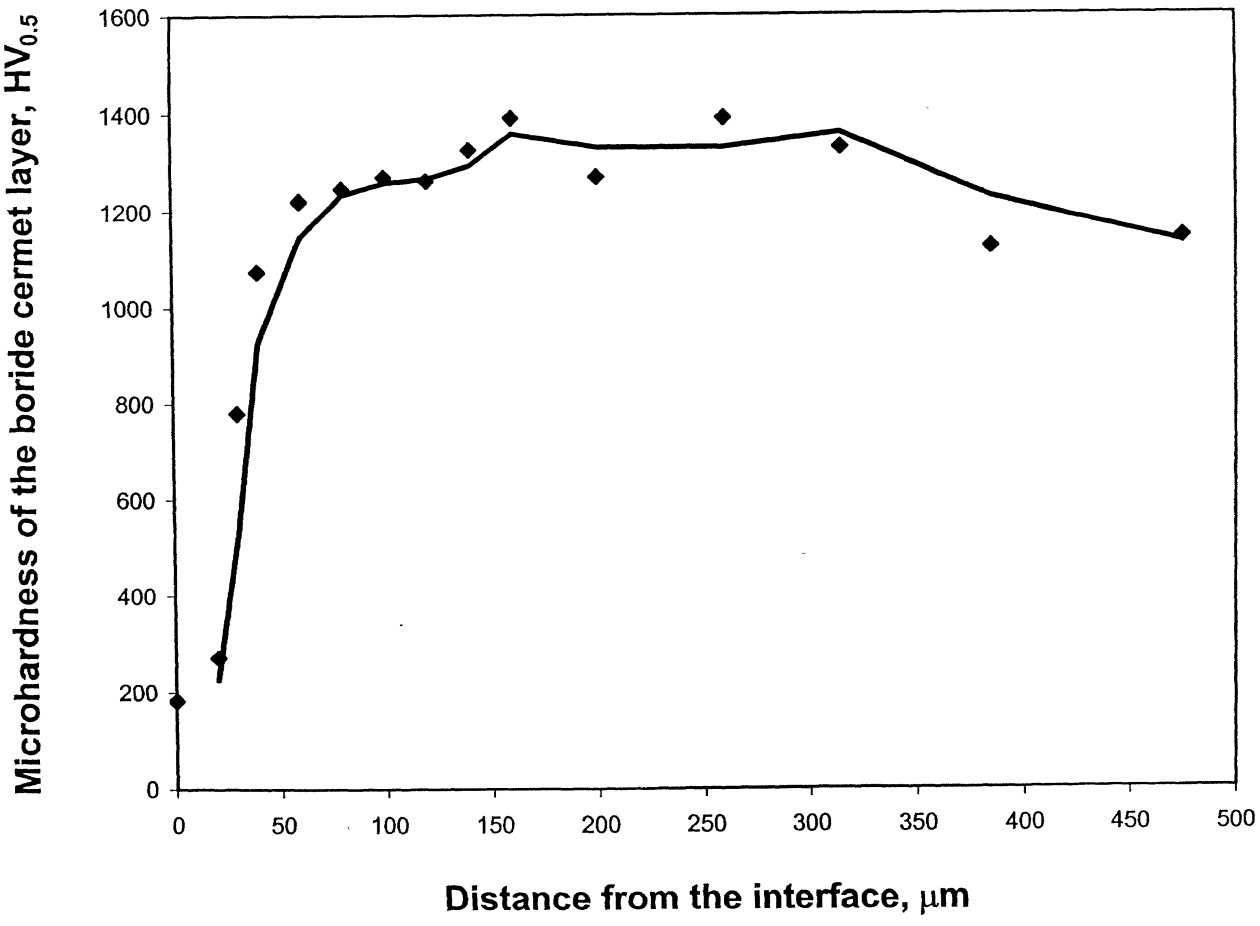

Figure 3.8 Microhardness variation in the sinter bonded cermet region from cermet / steel interface.

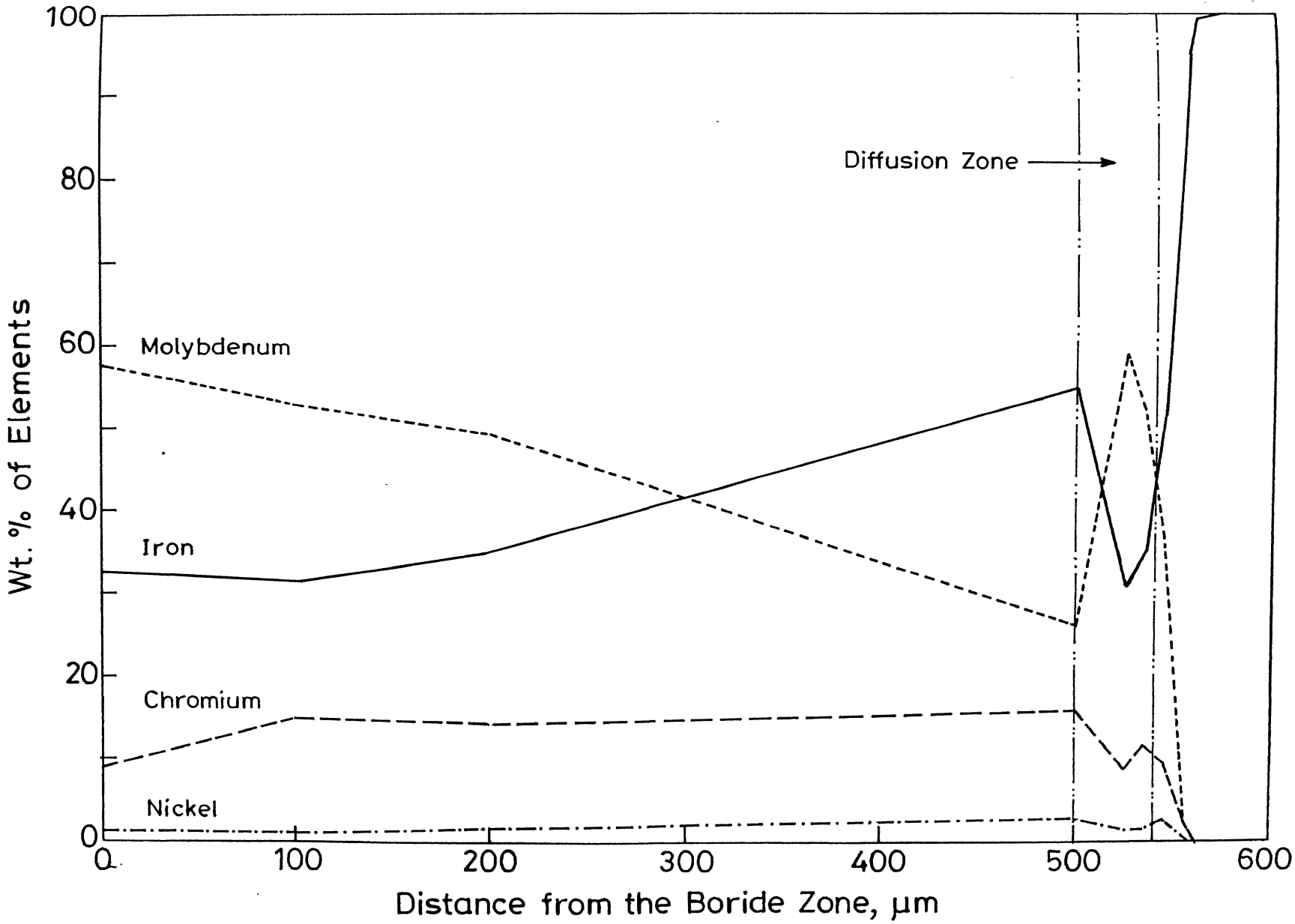

Figure 3.9 EPMA of sinter bonded cermet across cermet / steel diffusion zone.

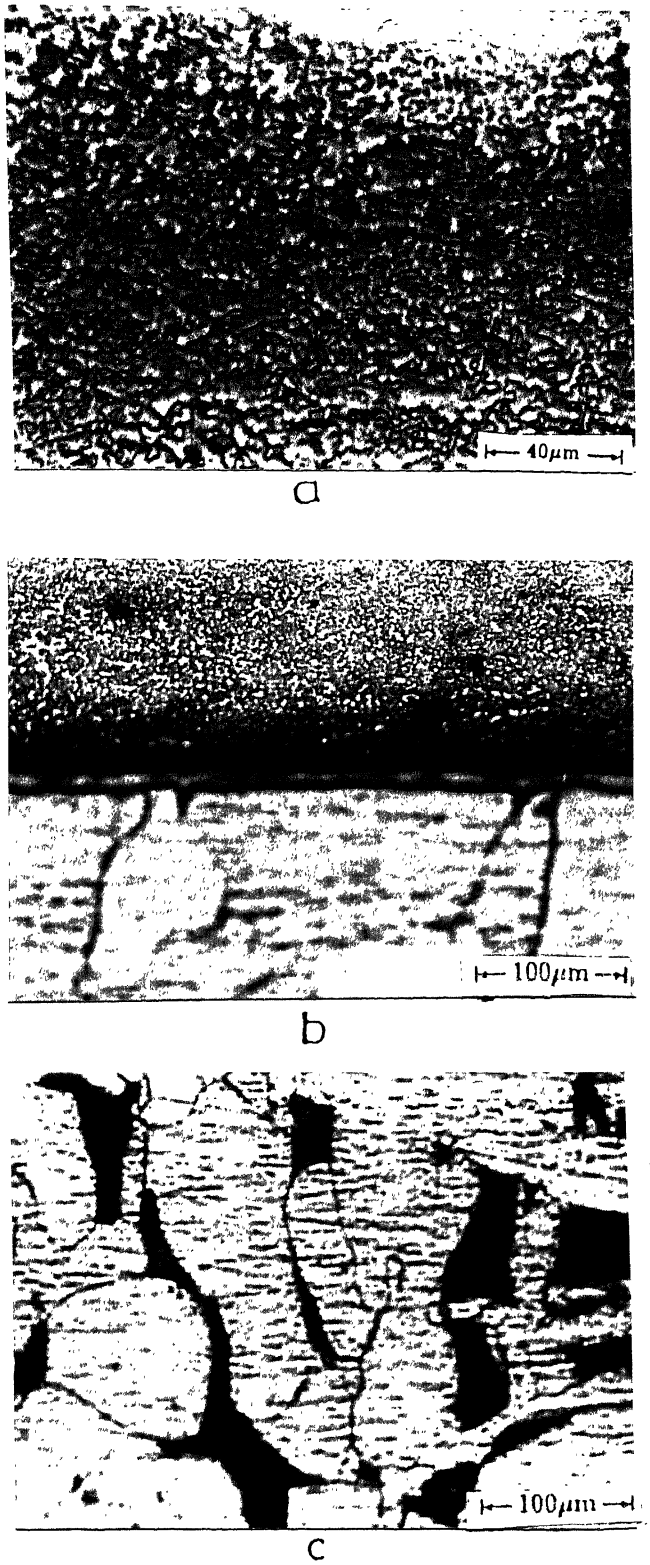

Figure 3.10 Optical microstructures of sinter bonded boride cermet onto steel (sample 1, Table 3.3).

(a) cermet cladding,
(b) overall view cermet / steel interface,
(c) steel substrate.

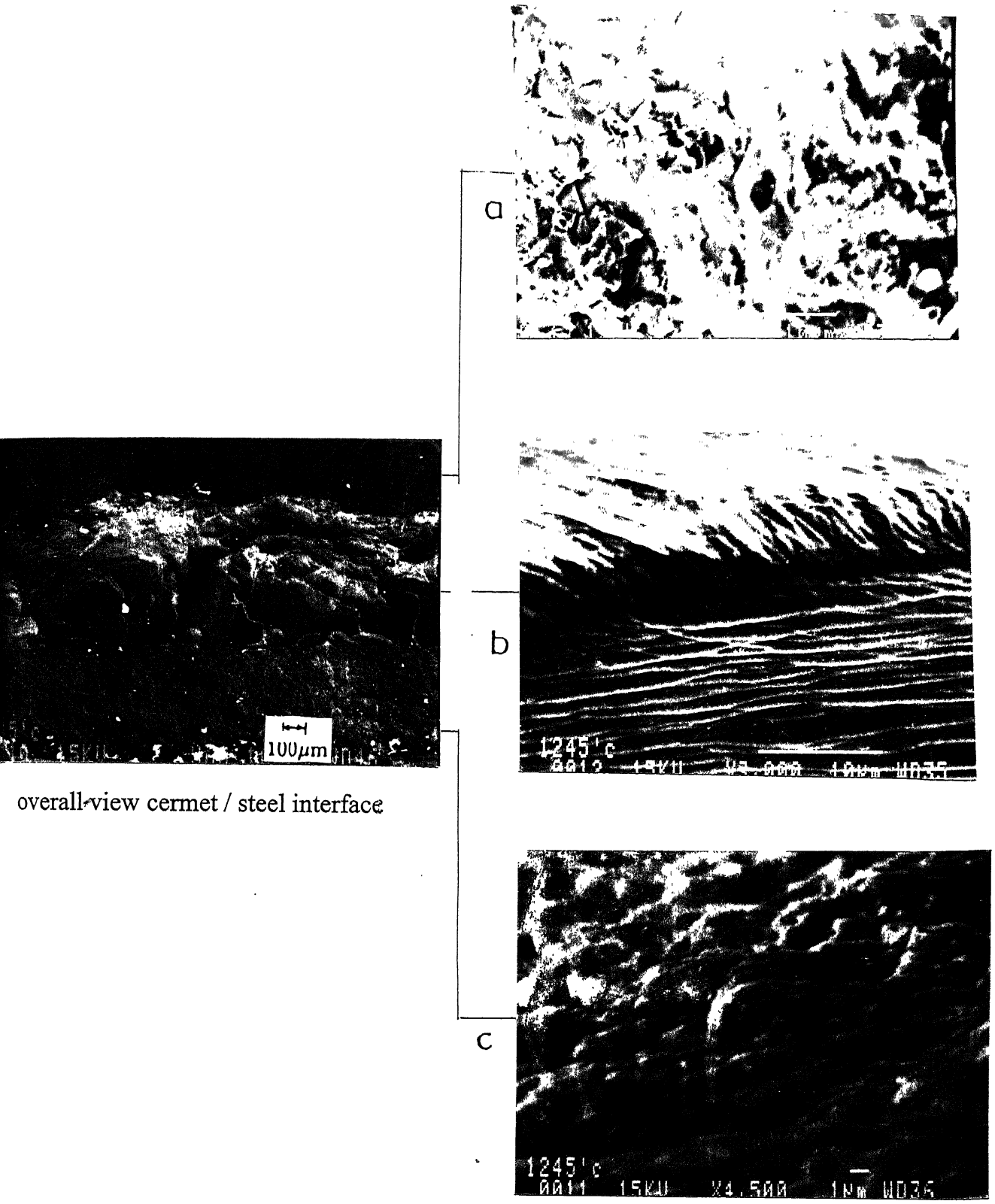

Figure 3.11 SEM fractographs of sinter bonded boride cermet onto steel (Sample 1, Table 3.3) after tensile testing.

(a) cermet cladding,
(b) diffusion zone of cermet / steel interface,
(c) steel substrate.

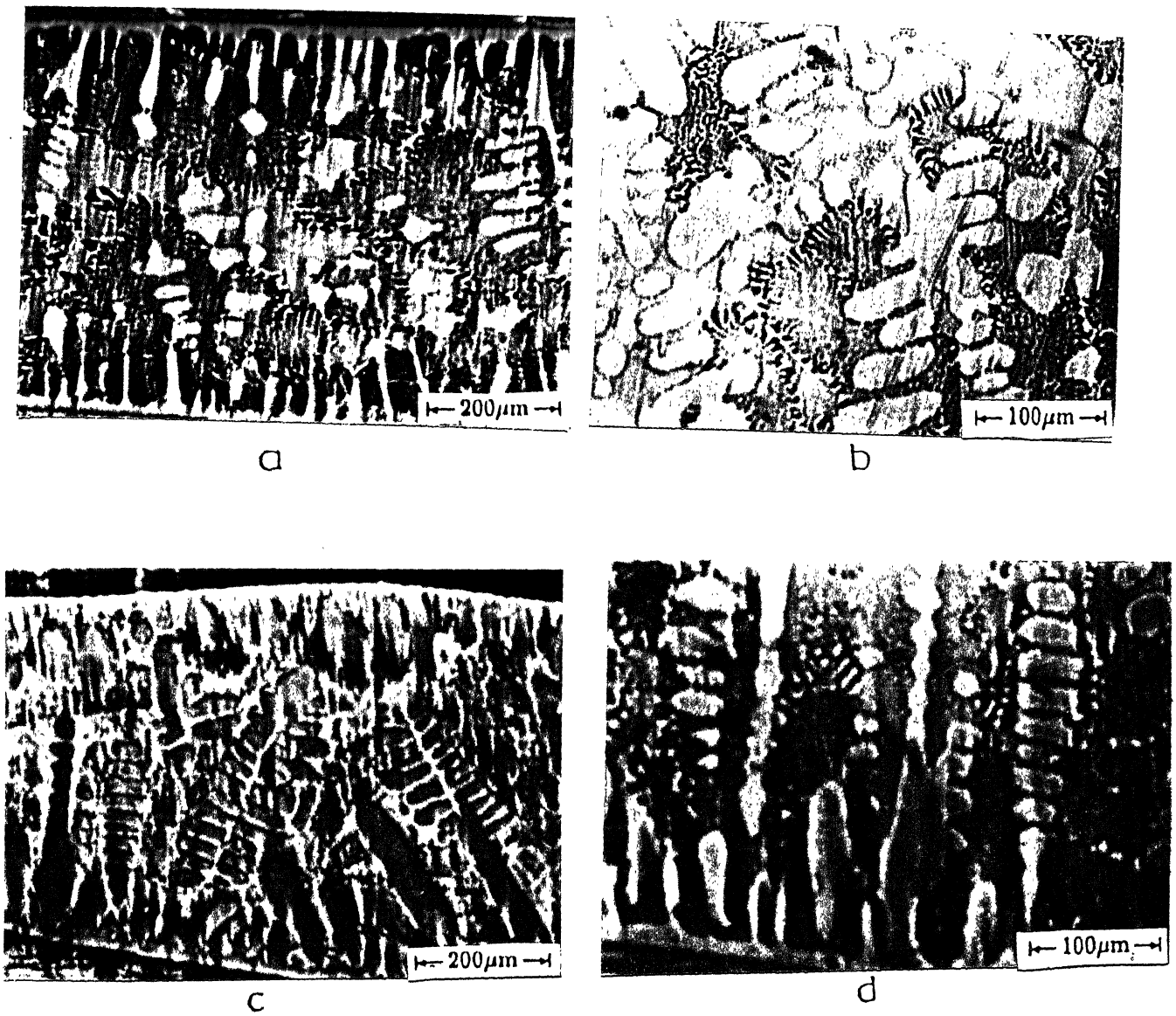

Figure 3.12 Optical micrographs of sandwiched boride cermet layer of different thickness between two steel plates.

(a) and (b), Sample with thicker boride cermet layer between steel plates (Sample 2, Table 3.3).

(c) and (d), Sample with thinner boride cermet layer between steel plates (Sample3, Table 3.3).

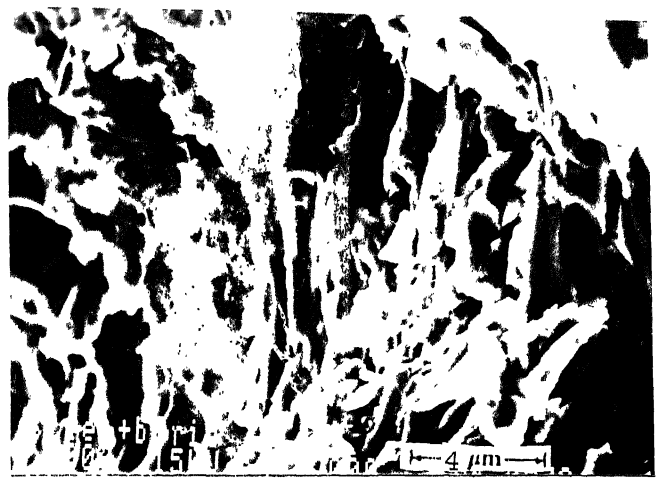

a

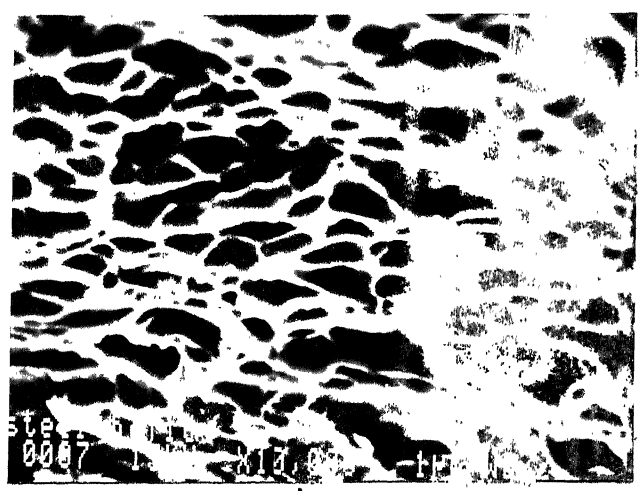

b

Figure 3.13 SEM fractographs of sandwiched boride cermet layer between two steel plates (Sample 2, Table 3.3), after tensile testing.
(a) boride cermet region.
(b) diffusion zone of cermet / steel interface.

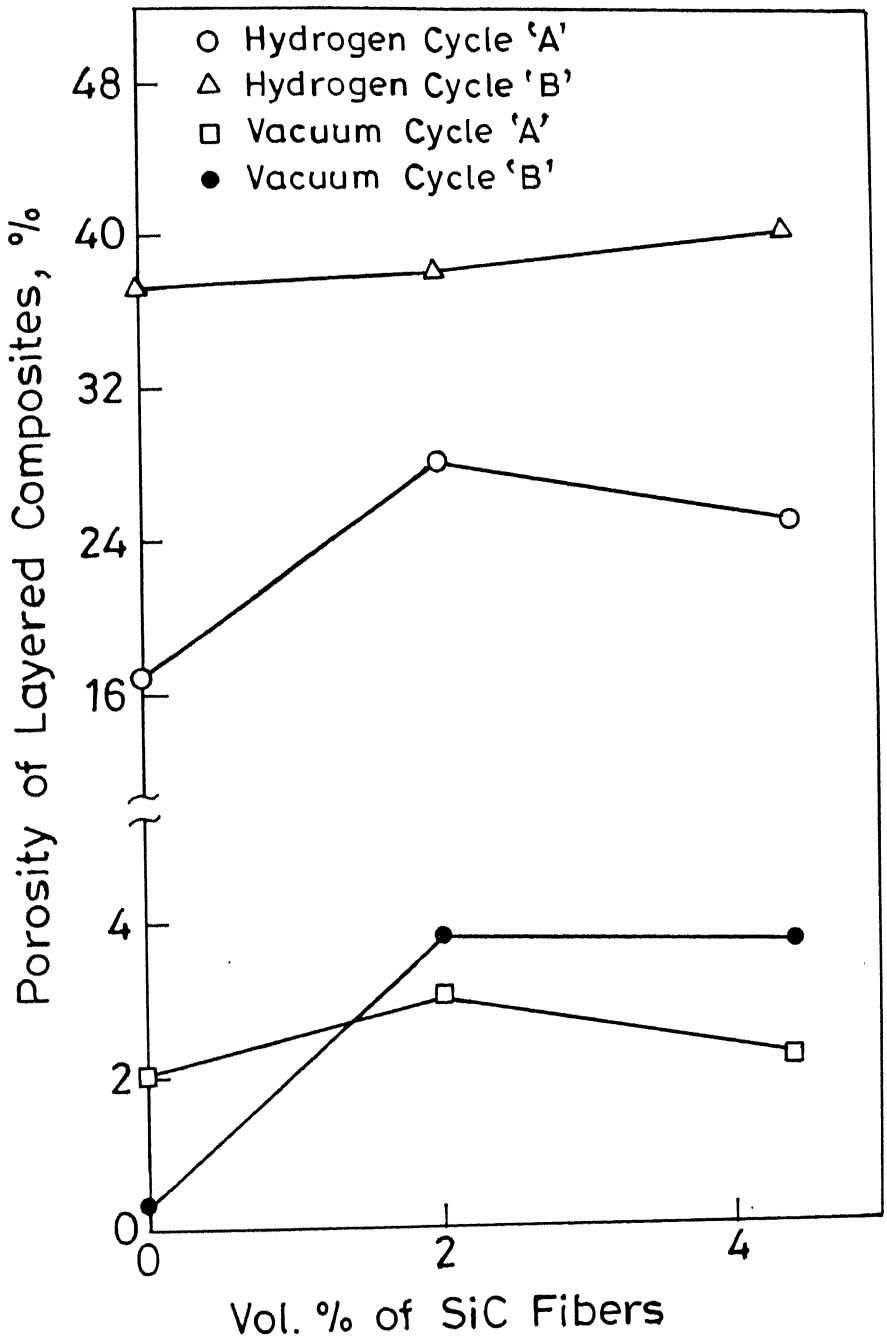

Figure 3.14 Variation of percentage porosity in composites with volume percent of SiC fibers and sintering cycles.

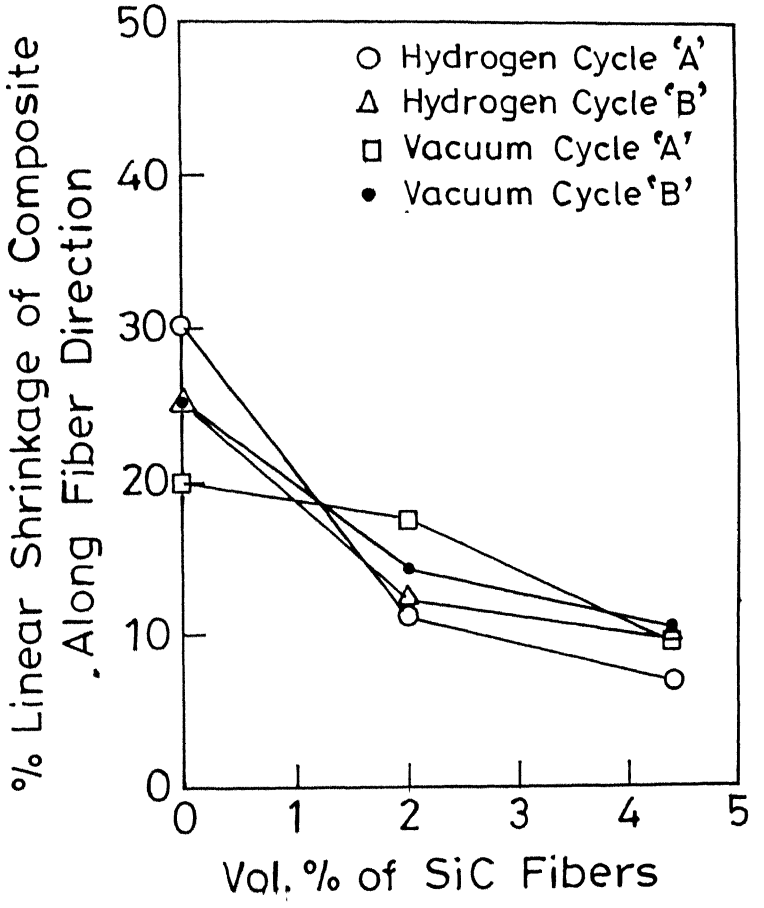

Figure 3.15 Variation of linear shrinkage of the composites in fiber direction with volume percent of SiC fibers and sintering cycles.

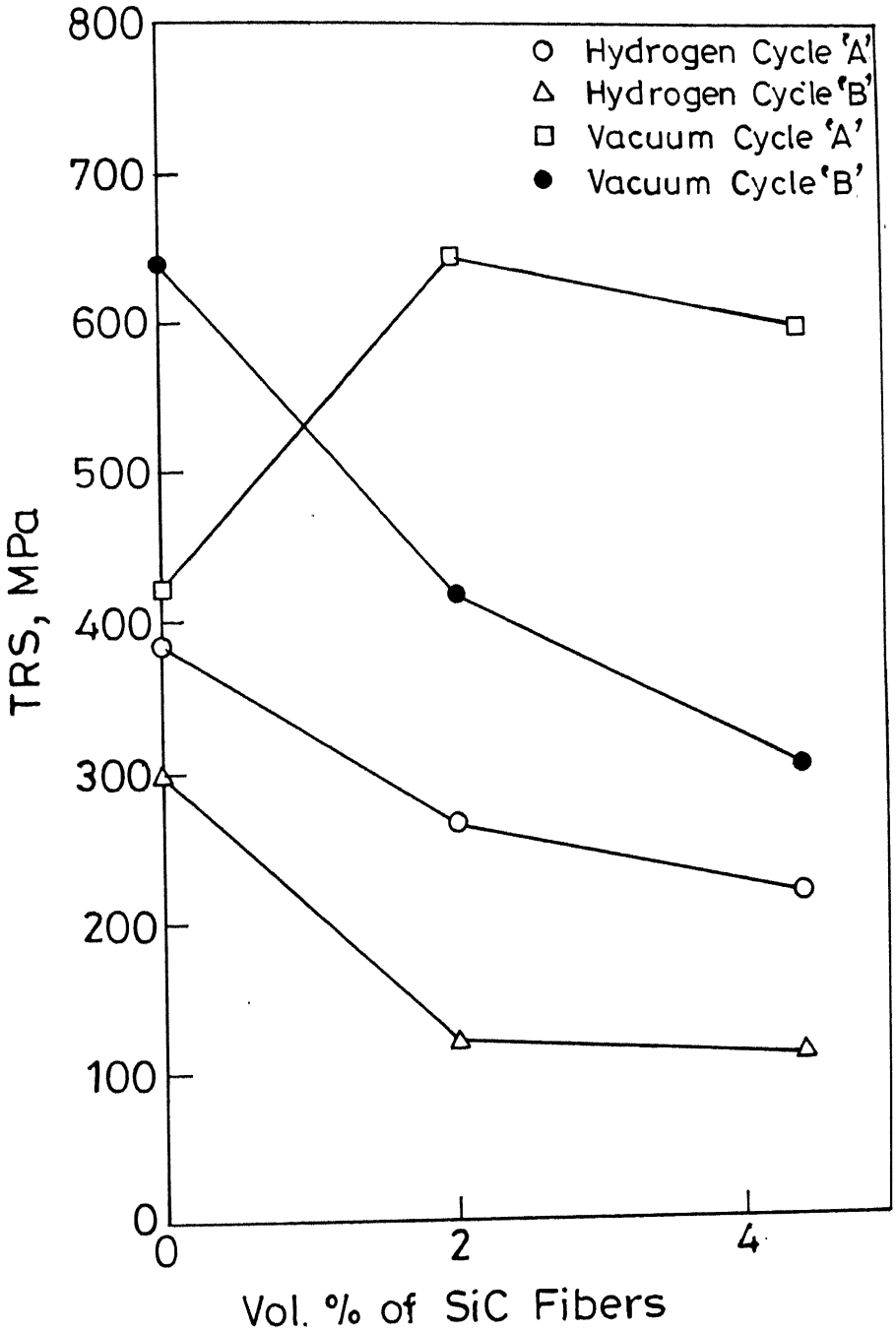

Figure 3.16 Variation of TRS of composites with volume percent of SiC fibers and sintering cycles.

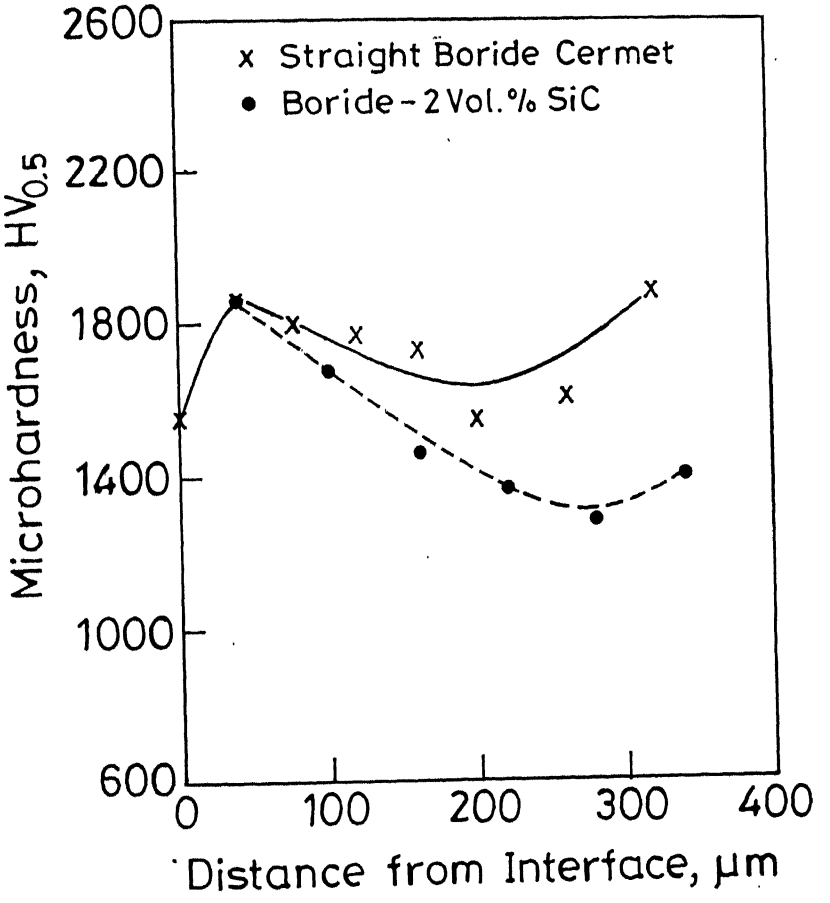

Figure 3.17 Variation of microhardness in 2 Vol. % SiC composite across the interface containing SiC fibers.

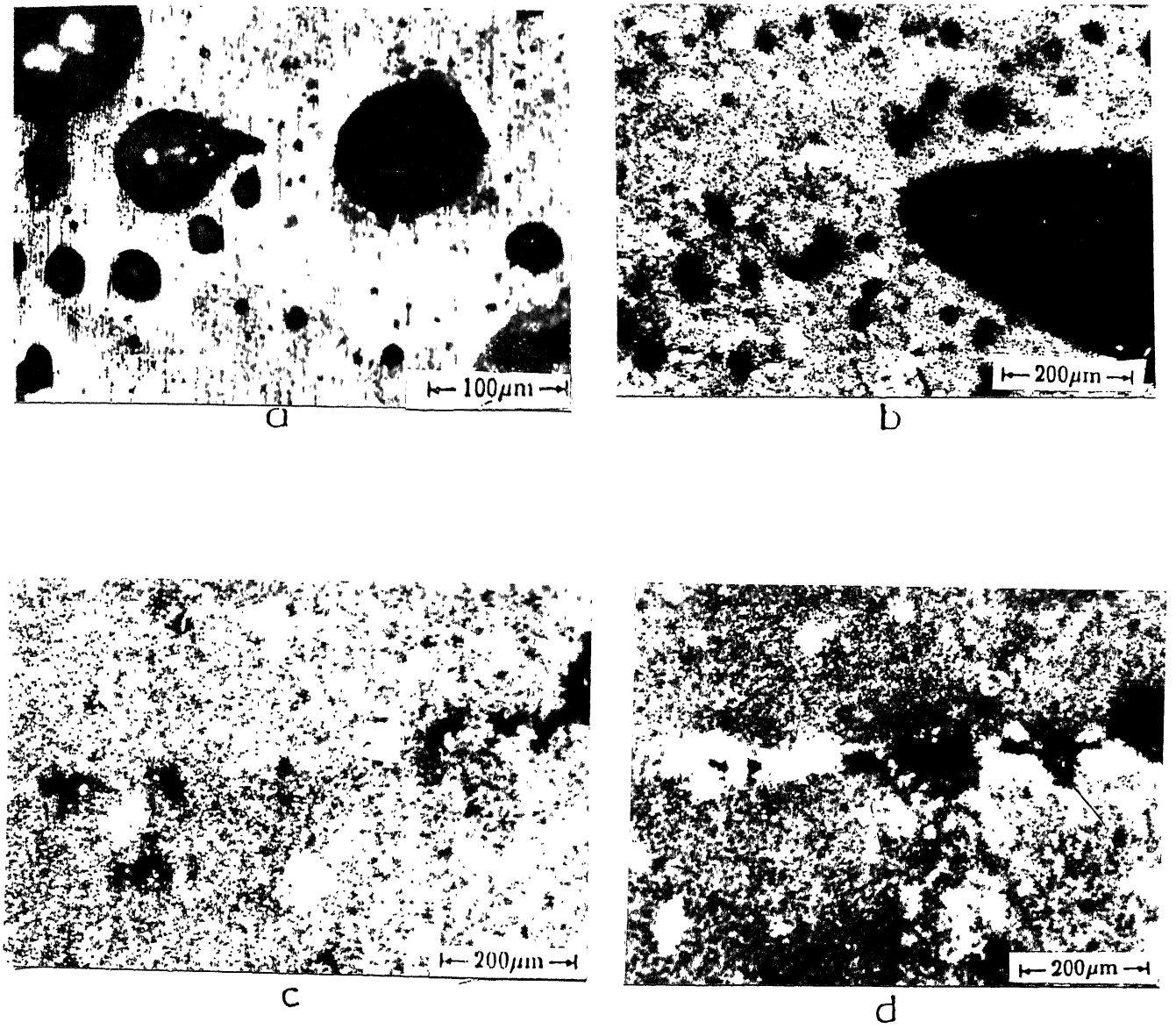

Figure 3.18 Optical micrographs of lamellar boride cermet composites containing different volume percent of SiC fibers.
(a) 2 % SiC, hydrogen sintered (Sample 6, Table 3.1),
(b) 4.4 % SiC, hydrogen sintered (Sample 5, Table 3.1),
(c) 2 % SiC, vacuum sintered (Sample 3, Table 3.2),

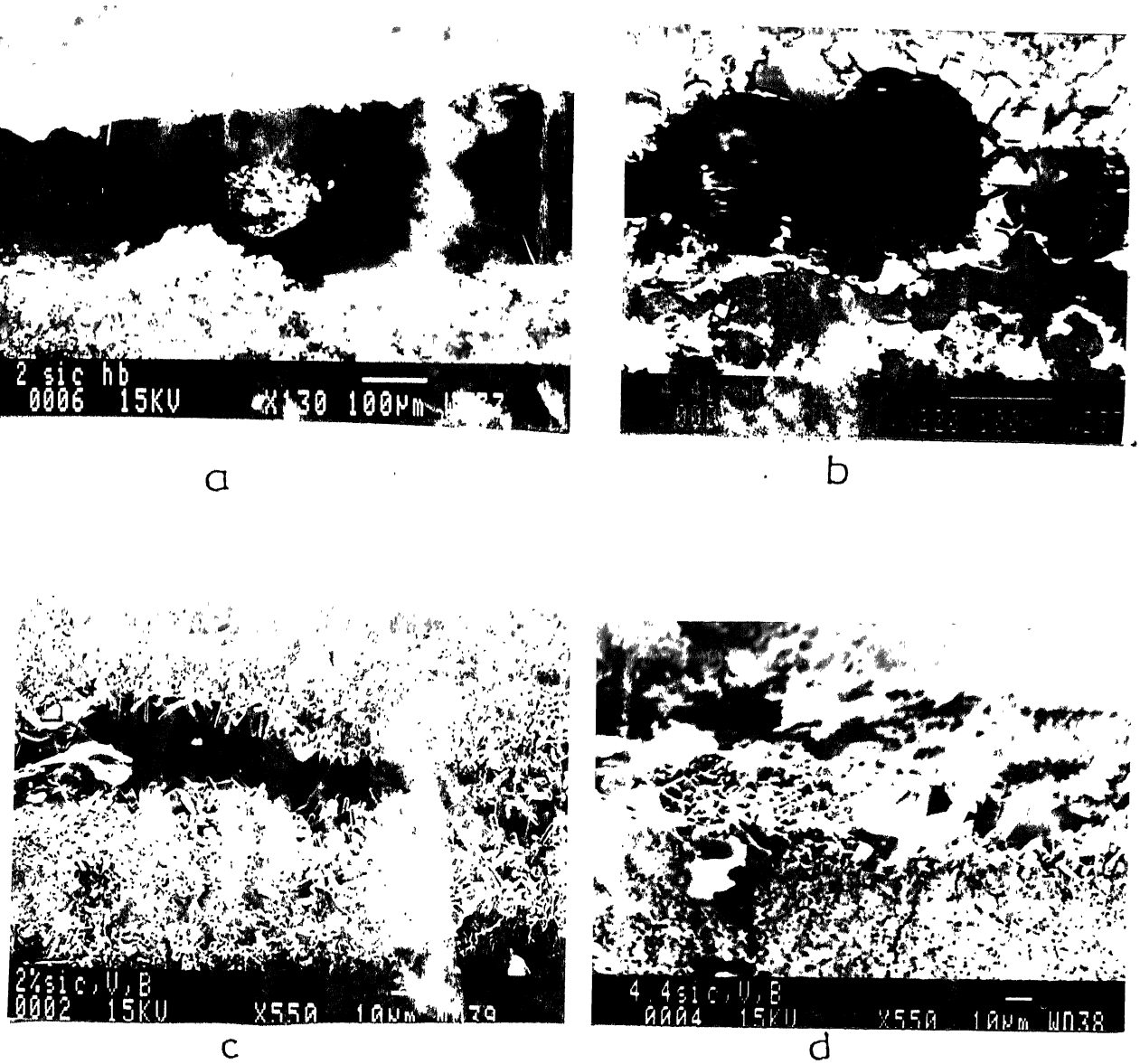

Figure 3.19 SEM fractographs of lamellar composites containing different volume percent of SiC fibers and sintered in different atmosphere.
(a) 2 % SiC, hydrogen sintered (Sample 13, Table 3.1),
(b) 4.4 % SiC, hydrogen sintered (Sample 14, Table 3.1),
(c) 2 % SiC, vacuum sintered (Sample5 , Table 3.2),
(d) 4.4 % SiC, vacuum sintered (Sample 6, Table 3.2).

Chapter – 4

Discussion

The results of the present investigation have been discussed in three sections. Section 4.1 deals with the sintering parameters and properties of boride cermet. Section 4.2 discusses the sinter bonding of boride cermet layer on to steel substrates. While in the Section 4.3 the processing / property relations of layered composites of boride cermet with SiC fibers have been discussed.

4.1 Sintering of Boride Cermet (KH-C50): -

4.1.1 Interlamellar Binder (PVA)

Presence of Poly Vinyl Alcohol (PVA) solution, at the interface between boride cermet lamellae during green compaction not only facilitate the green sample handling, but also helps in attaining better bonding (Sample 1 and 2, Table 3.1). This binder layer holds the boride cermet lamellae sticked together minimizing the interlayer air entrapment in the green compact. Complete removal of this binder is certain in debinding stage (400 °C) of sintering cycle. Development of better interface after PVA application is confirmed by optical micrographs (Fig. 3.4 (a) and (b)). A marginal

improvement in TRS also confirms better interfacial bonding (Sample 1 and 2, Table 3.1).

4.1.2 Number of Boride Cermet Layers

For the purpose of increasing thickness of final sintered samples, the number of layers being stacked over one another can be increased (Sample 3, Table 3.1). But it increases the percentage porosity of the sample, mainly due to the increased possibility of air entrapment between the lamellar interfaces. The fall in the TRS is correlated with increase in porosity (Sample 2 and 3, Table 3.1).

4.1.3 Sintering Atmospheres and Cycles

It is well known that boride cermet (KH-C50) can be sintered either in vacuum or reducing atmosphere (hydrogen). When the cermet is sintered in hydrogen (Sample 2, Table 3.1), percentage porosity (16.7 %) is much higher compared to that sintered in vacuum (2 %) (Sample 1, Table 3.2). As vacuum is effective in drawing out the entrapped air, it reduces percentage porosity and hence improves interlamellar bonding between the boride layers. This variation in porosity affects the mechanical properties of cermet. Cermet sintered in vacuum has TRS value of 421 MPa compared to 378 MPa of hydrogen sintered cermet. Still the TRS value obtained is much lower than maximum reported value of 1.6 – 2.0 GPa [3, 11]. The difference can be attributed to

sample size being tested. Samples in the present investigation are much thinner (1.0 – 1.5 mm) as compared to 4.0 – 4.85 mm selected in the earlier investigations [3, 11]. The presence of even a minor flaw or surface irregularity would severely affect the strength in thinner cross-sections.

Similar to TRS values, the macrohardness and microhardness values of the cermets sintered in vacuum are more than those sintered in hydrogen (Fig. 3.1). This directly reflects the effect of porosity on the strength of sintered cermet.

When two different cycle 'A' and cycle 'B' (Section 2.3, Fig 2.1) were employed, the results obtained for hydrogen and vacuum are opposite. When the cycle 'B' was employed in vacuum (Sample 2, Table 3.2), better densification than cycle 'A' was observed (Sample 1, Table 3.2). Moreover cermets sintered according to cycle 'B' in vacuum shows higher TRS (636.1 MPa) than those sintered according to cycle 'A' (421.0 MPa). The improvements are attributed to better debinding, and reduction of oxides at isothermal hold at 1000 °C for 60 min. But when the cycle 'B' was followed in case of hydrogen sintering (Sample 12, Table 3.1), densification and TRS of the cermets got deteriorated as compared to samples sintered as per cycle 'A' (Sample 2, Table 3.1). The reason behind this reversal is not very clear.

The grain shape and size of ternary boride phase do not show significant difference in either of sintering cycles or atmospheres. This confirms that variation in mechanical properties is primarily due to change in percentage porosity.

4.1.4 X-ray Diffraction Analysis

XRD plots (Fig. 3.2) give an account of phase changes occurring during reaction sintering of KH-C50. In the green form, XRD plot shows molybdenum and iron in their elemental state and FeB as compound. In the XRD of sintered cermet almost all the diffraction peaks correspond to Mo_2FeB_2 ternary boride. Disappearance of molybdenum and FeB peaks corresponding to green sample after sintering confirms the reactive nature of sintering. Chromium forms a substituional solid solution with Mo_2FeB_2 resulting in to $(Mo, Fe, Cr)_3B_2$ phase, whose presence has been confirmed by earlier investigators [12].

4.2 Sinter Bonding Boride Cermet onto Steel Substrate

4.2.1 Densification Behaviour

The sinter bonding between boride cermet KH-C50 and steel is similar to Transient Liquid Phase Bonding (TLPB), except the eutectic liquid phase of iron –boron at the interface is not transient in nature. In the present

investigation all reported experiments have been carried out in hydrogen atmosphere as per cycle 'A' only. The process of sinter bonding could not be optimized in vacuum. This may be due to relatively poor vacuum generated by the system. When the steel plate is cladded with KH-C50 lamella (Sample 1, Table 3.3), the total porosity is lowest. Optical micrograph (Fig. 3.10 (b)) shows absence of pores or irregularities at the interface. A thin uniform diffusion layer shows formation of ideal bonding. On the other hand samples having sandwiched KH-C50 lamella between the steel plates (Samples 2 and 3, Table 3.2) have almost double the amount of sintered porosity. The reason may be attributed to the fact that the steel plates act as a non-permeable shell to the entrapped air in the KH-C50 layer. Sintering in the hydrogen cannot encourage this entrapped air to escape fully. In many cases it gets merged into rather very big pores visible by naked eye at the fractured cross-sections. In case of sample with thinner KH-C50 lamella sandwiched between two steel plates (Sample 3, Table 3.3), the presence of pores was more pronounced and its bonding is poorer than sample having thicker boride layer.

Observation of linear shrinkage of the cladded cermet layer shows some interesting trends. The cladded KH-C50 layer on to steel substrates (Sample 1, Table 3.3) experiences shrinkage in all linear dimensions. While in the case of samples having sandwiched KH-C50 layer (Samples 2 and 3, Table 3.3), the

steel strip, placed above KH-C50 layer acts as a minor external load during sintering. Presence of liquid phase at the interface and the external pressure along the thickness causes greater amount of shrinkage in that direction. In all the (Samples1-3, table 3.3) the volumetric shrinkage of boride cermet (KH-C50) layer is more or lees constant confirming equal extent of densification.

4.2.2 Mechanical Properties

When an inherently brittle material like boride based cermet, is cladded over to steel substrates the ultimate tensile strength of the cladded steel is bound to fall. It is exactly what is observed presently (Fig. 3.6). Heating of steel in hydrogen, while placing it over the graphite boat causes carburisation of steel, which was confirmed metallographically. It is depicted in the variation of microhardness, UTS, and percentage elongation after heating (Fig. 3.7).

4.2.3 EPMA Study of Cermet / Steel Diffusion Zone

In the sinter bonding process there exists a concentration difference of elements between boride cermet (KH-C50) and steel. The KH-C50 is richer in boron, molybdenum, chromium and nickel, which tend to diffuse to steel to equilibrate the concentration difference. The EPMA results (Fig. 3.9) show that molybdenum and iron are actively involved in interface build up. The presence of nickel and chromium in the cermet is fairly constant up to the interface after which their presence vanishes sharply. This indicates the passiveness of the

nickel and chromium in the eutectic melt formation. It is noteworthy that concentration of iron increases as one moves closer to cermet / steel interface. Proposed explanation for this is as under. The driving forces for the formation of melt and dissolution of iron based substrate is supplied by the initial infinite boron concentration difference prevailing across interface [30–33]. The eutectic liquid formed at cermet – steel interface at around 1200 °C [22], is drawn into the interfacial pores of cermet by capillary action [26]. Further the chemical similarity of iron –boron eutectic melt with cermet makes it wettable. Such an iron rich liquid is confirmed from EPMA results.

4.2.4 Microstructural Studies

The interface between boride cermet cladding and the steel (Sample 1, Table 3.3) is distinctly visible (Fig. 3.10 (b)). Few of the finely distributed boride grains are coalesced. In case of sandwiched boride cermet layer between steel plates (Sample 2 and 3, Table 3.3), the iron based binder phase seems to be directionally solidified in the form of dendritic grains and the boride grains are lumped together as a dark phase. This dendritic grain growth of the binder phase may be attributed to the directional cooling experienced by the cermet layer. The thermally conducting steel plates enclosing the boride layer extract heat as sintering cycle ends, which causes directional solidification of binder

phase in the cermet. The microstructural homogeneity of the cermet is deteriorated due to this phenomenon.

The SEM fractographs (Fig. 3.11) of KH-C50 cladded steel sample (Sample 1, Table 3.3) show brittle and ductile fracture of cermet cladding and steel substrate respectively. The magnified view of the diffusion layer (Fig. 3.11 (b)) shows the directionally grown microstructure, which is due to heat flow in the preferred direction during solidification. In case of sandwiched boride layer (Sample 2, Table 3.3) cermet – steel interface shows a relatively ductile cellular type microstructure (Fig. 3.13 (b)). This clearly manifests that at interface there is a relatively larger volume fraction of melt which give the wider possibility of formation of cellular type microstructure.

4.3. Sintering of Layered Composites of Boride Cermet with SiC Fibers

4.3.1 External Load During Sintering

As already described the densification of boride cermet (KH-C50) proceeds through liquid phase sintering. Presence of external pressure during sintering has little effect over densification of the straight cermet. Presently it is observed that a minor external load (~200 Pa) helps in controlling distortion and enhancing interlamellar bonding (Sample 4 and 5, Table 3.1). It does so by reducing the possibility of air entrapment from the interface.

4.3.2 Effect of Volume Fraction of SiC Fibers

Introduction of fibers between cermet lamellae invariably increases the porosity as compared to straight cermet sintered in same atmosphere and cycle (Fig.3.14). SiC fibers at the lamellar interface hinder the bonding process due to non-wetting characteristics of the boride cermet with the fiber. On increasing the volume fraction of the fibers to 4.4 %, the increased irregularities at the interface are evident from the optical micrographs (Fig. 3.18) and hence the interlamellar bonding deteriorates. It results in lowering of TRS of fiber reinforced composites as compared to the straight cermets (Fig. 3.16). The only exception being the samples sintered in vacuum cycle 'B, the reason, for which, is not clear. Presence of larger volume fraction of the melt at fiber containing interface is clearly visible in the micrographs (Fig. 3.18). The presence of fibers at the interface might also develop some stress field in the contacting cermet body, which enhances liquid phase formation. In order to avoid much fiber to fiber clustering, a multi layered fibrous composite was tested (Sample 10, Table3.1), but it was observed that increase in number of interfaces resulted in more air entrapment leading to still lowering of TRS (Sample 6, Table3.1). The effect observed is similar to one discussed in case of straight lamellar cermets (Section 4.1.2). An excessive volume percent of fibers e.g. 25 % (Sample 11, Table 3.1) completely distorts the sample.

Fig. 3.15 illustrates that when the fibers are introduced between the cermet lamellae, the shrinkage of composites along the fiber laying direction drops maximum, as compared to the shrinkages along other two directions of the composites i.e. width and thickness. This shrinkage anisotropy in the composites was observed irrespective of the sintering atmosphere and cycle. The reason may be due to the fact that fibers touching the cermet layer hinder the cermet shrinkage along the direction of maximum contact. This hindrance will be more if the number of fibers in contact with cermet interface is more. This justifies further drop in longitudinal shrinkage of the composites with increase in the volume fraction of the fiber.

The microhardness studies on the 2 % SiC composite (Sample 3, Table 3.2) and the straight boride cermet are discussed in Section 3.3.3. As one traverses from the interface there is some increase in microhardness followed by a fall. However, it is not clear why the microhardness of SiC fiber containing interface is lower than that for straight boride cermets, althrough the hard fiber phase should increase the hardness. This appears due to the fact that there is some interfacial porosity in case of SiC fibers, which put cause a decrease in hardness.

4.3.3 Interlamellar Metallic Additives

In order to improve wetting between SiC fibers and cermet, metallic powders of aluminum, aluminum bronze and copper were applied respectively at the interface containing SiC fibers. The sample containing 2 vol. % of aluminum powder as an interlayer additive in 2 vol. % SiC composite yielded very poor bonding and was fragile in nature (Sample 7, Table 3.1). Aluminum bronze (Sample 8, Table 3.1) gave better results than pure aluminum, while copper powder gave even better TRS value (Sample 9, Table 3.1). The fractograph of the sample containing interlayer additive (Fig. 3.20) shows the non-wetting nature of additive. Literature confirms higher angle of contact between refractory borides and the metallic melt [25]. The failure of these interlayer additives confirms the application of the boride based cermet parts to hot metal dies and extrusion equipments for aluminum, copper and their alloy [17].

4.3.2 Sintering Atmospheres and Cycles

As discussed in section 4.1.3 the sintering atmosphere strongly affects the sintered porosity. The layered fibrous composites sintered in vacuum (Sample 3-6, Table 3.2) has considerably lower sintered porosity, compared to that sintered in hydrogen (Sample 5-6, 13-14; Table 3.1). The porosity variation in the composites (Fig 3.14) affects its mechanical properties. A

higher amount of porosity deteriorates strength. This is the reason why hydrogen sintered composites invariably, have lower TRS values than those sintered in vacuum. The fractographs show (Fig 3.19 (a) and (b)) poor interlamellar bonding in hydrogen sintered composites than the composites sintered in vacuum (Fig 3.19 (c) and (d)).

As evident from Fig 3.14, cycle 'B' sintered composites have higher percentage porosity compared to those sintered as per cycle 'A', for any selected sintering atmosphere. As discussed in section 4.1.3, the cycle 'B' has negative effect in hydrogen atmosphere. But as far as composites are concerned, cycle 'B' sintered composites have lower TRS than those sintered according to cycle 'A' (Fig. 3.16). This is in accordance with porosity levels of the composites (Fig. 3.14).

Chapter – 5

Conclusions

Following conclusions can be drawn from the present investigation.

1. Poly Vinyl Alcohol (PVA) as binder during green compaction helps in attaining better interlamellar bonding.
2. On increasing the number of cermet layers being staked, the porosity in the layered straight boride cermet compacts increases.
3. Vacuum sintered cermets have better densification and hence better mechanical properties than hydrogen sintered ones.
4. Mo_2FeB_2 ternary boride grains have rectangular facet morphology and average grain size of less than 3 μm, which shows insignificant variation in cermet, sintered in either of atmospheres and cycles.
5. Sinter bonding process involves formation of interfacial iron–boron eutectic melt formation. The process is sensitive to presence of oxides at the interface. A good vacuum or reducive atmosphere is needed.
6. Presence of alloying additions such as nickel and chromium do not have significant role in interface build up during sinter bonding.
7. A relatively rapid cooling after sintering promotes directional solidification of the binder phase.

8. An imposed minor external load (~200 Pa) during sintering of SiC fibrous composites helps in reducing distortion and air entrapment in the composite.

9. Presence of fibers in the boride cermet composites lower the shrinkage of composites in the fiber lay direction as compared to straight cermet. On increasing the fiber content of the composite, the lengthwise shrinkage falls further irrespective of the sintering atmosphere and cycle.

10. Presence of SiC fibers at the interface hinders in bonding. 2 vol. % SiC fiber composite usually have higher porosity and lower TRS than the straight cermet. On increasing SiC fiber content in the composite the TRS invariably falls.

11. Vacuum sintered fibrous composites have better densification and TRS than hydrogen sintered composites. In case of hydrogen sintering, cycle 'A' gave better densification and TRS than cycle 'B'.

12. Interlamellar metallic additives e.g. copper, aluminium and aluminium-bronze invariably reduces the TRS of the composite due to their poor wetting in cermet-fiber system.

CENTRAL LIBRARY
I. I. T., KANPUR
Acc. No. A 132011

References

1. R. Thompson, "The chemistry of metal borides and related compounds", Progress in Boron Chemistry, Vol. 2, Edited by R. J. Brotherton and H. Steinberg, Pergamon Press, Oxford, 1970, pp. 173-230.

2. K. Takagi, M. Komai, and S. Matsuo, "Development of ternary boride base cermets", Powder Metallurgy Proceedings of World Congress'94, Vol. 1, 1994, pp. 227-234.

3. K. Takagi, S. Ohira, T. Ide, T. Watanabe, and Y. Kondo, "New multiple boride based hard alloys", Modern Developments in Powder Metallurgy, Vol. 16, Edited By E. N. Aqua and C. I. Whitman, Metal Powder Industry Federation, Princeton, 1985, pp. 153 – 166.

4. M. Komai, Y. Sobe, S. Ozaki, and K. Takagi, "Properties and microstructures of WCoB base cermets", PM'93, Kyoto, July 1993.

5. M. Komai, Y. Yamanasaki, and K. Takagi, "Sintering behaviour of a reactive sintered ternary boride base cermet", Solid State Phenomena, Vol. 25-26, 1992, pp. 531-538.

6. T. Ide, M. Fukumori, K. Takagi, T. Watanabe, and Y. Kondo, "Sintering behaviour of an iron containing multiple boride base hard alloy", Horizons of Powder Metallurgy II, Proceedings of the 1986 International Powder metallurgy conference and exhibition "The Future of Powder Metallurgy" PM'86, Edited By W. A. Kaysser and W.J. Huppmann, pp. 1073-1076.

7. K. Takagi, M. Komai, T.Ide T. Watanabe, and Y. Kondo, "Characteristics of the Mo_2FeB_2 type hard phase in an iron containing multiple boride based hard alloys", ", Horizons of Powder Metallurgy II, proceedings of the 1986 International Powder metallurgy conference and exhibition "The Future of Powder Metallurgy" PM'86, Edited By W.A. Kaysser and W.J. Huppmann, pp. 1077-1080.

8. K. Takagi, T. Watanabe, T. Ando, and Y. Kondo, "Effect of Mo and carbon on the properties of iron molybdenum boride hard alloys", The International Journal of Powder metallurgy, Vol. 22, No. 2, 1986, pp. 91-96.

9. K. Takagi, M. Komai, T. Ide, T. Watanabe and Y. Kondo, "Effect of Mo and Cr contents on the properties and phase formation of iron molybdenum boride base hard alloys" Powder Metallurgy International, Vol. 19, No. 5, 1987, pp 30-33.

10. T. Ide, K. Nakano, T. Ando, "Effect of Mo and Sintering Temperature on the strength, hardness, and density of Fe-6 mass % B-x mass % Mo alloys", Powder Metallurgy International, Vol. 20, No.3, 1988, pp. 21-24.

11. K. Takagi, M. Komai, T. Ide, T. Watanabe, and Y.Kondo, "Effect of Ni on the mechanical properties of Fe, Mo, Boride hard alloys", The International Journal of Powder Metallurgy, Vol. 23, No. 3, 1987, pp. 157-161.

12. T. Ide and T. Ando, "Reaction sintering of an Fe-6 wt %B-48 wt % Mo alloy in the presence of liquid phases", Metallurgical Transaction A, Vol. 20A, Jan-1989, pp.17-24.

13. M.Komai, K. Takagi, T. Watanabe, and Y. Kondo, "Effect of Co on the properties and phase formation of Mo_2FeB_2Complex boride base hard alloys", Boron Rich Solids, Edited By D. Emin, T. L. Aselage, A. C. Switendick, B. Morosin and C. L. Beckel, American Institute of Physics, New York, pp. 578-581.

14. K. Takagi, M. Komai, T. Ando and Y. Kondo, "The microstructure and properties of sintered Mo_2FeB_2 base hard alloys", Sintering' 87, Vol. 2, Edited By S. Somiya, M. Shimada, M. Yoshimura and R. Watanabe, Elsevier Science Publishers Ltd., 1988, pp. 1296-1301.

15. K. Sivaraman, A. Griffo, R. M. German, K. Takagi, "Development of ternary boride cermet for high wear resitant applications", Advances in Powder Metallugy and Particulate Materials, Compiled By T. M. Cadle and K. S(Sim). Narasimhan, Metal Powder Industries Federation APMI International, Princeton, New Jersy, 1996, pp. 11.67-11.80.

16. K. Takagi, "Applications of borides to wear resistant materials – ternary boride cermets", Japanese Journal of Applied Physics, Series 10, 1994, pp. 200-203.

17. K. Takagi, M. Komai, T. Watanabe, and Y. Kondo, "Applications of Mo_2FeB_2 complex boride base hard alloys to injection molding machine parts", Proceedings of PM'90, World Conference on Powder Metallurgy, The Institute of Metals, Vol. 1, 1990, pp. 374-384.

18. M. Komai,K. Takagi, T. Watanabe, and Y. Kondo, "Corrosion behavior of sintered Mo_2FeB_2 base hard alloys", Material Research Society International Meeting on Advanced Materials, Vol. 4, 1989, pp. 475-479.

19. A. P. Epik, "Boride coatings", Boron and Refractory Borides, Edited by V. I. Matkovich, Springer-Verlag Berlin Heidelberg, New York, 1997, pp. 597-611.

20. N. E. Dowling, "Mechanical behaviour of materials", Prentice-Hall, New Jersy, 1993.

21. C. J. Smithells, "Metal's Reference Book, Vol. 2", 3rd ed., Butterworth, London, 1962, pp. 702-703.

22. K. Sivaraman, "Reaction sintering of $(Mo, Fe, Cr)_3B_2$ ternary boride – a study on its phase evolution and sinter bonding onto steel substrates", M.S. Thesis, Dec 1996, The Pennsylvania State University, U.S.A.

23. P. K. Bagdi, "Processing and properties of $Mo_2Fe(Ni)B_2$-Fe(Ni) cermets", PhD Thesis, Dec 1995, Indian Institute of Technology, Kanpur, India.

24. K. Takagi, T. Kawamura, N. Sakamato, M. Fukumori, T. Watanabe, and Y. Kondo, "Junctionability of iron containing multiple boride base hard alloys", Iron and Steel Institute of Japan, 1985, Vol. 25, pp. B-376.

25. G. S. Upadhyaya, "Sintered metallic and ceramic materials – preparations, properties, and applications", John Willey and Sons Ltd., Chichester, 1999.

26. R. M. German, "Liquid phase sintering", Plenum Press, New York, 1985.

27. D.W. Richerson "Modern ceramic engineering – properties, processing and use in design", Marcel Dekker, inc; New York,1982.

28. B. D. Cullity, "Elements of X-ray diffraction", 2nd edition, Addison-Wesley Publishing, inc, Massachusetts, 1978.

29. 'Kohan's Hard Materials- KHM', Product Information Brochure, Toyo Kohan Co. Ltd., Tokyo, Japan.

30. I. Tuah–Poku, M. Dollar, and T. B. Massalaski, "A study of transient liquid phase bonding process applied to Ag/Cu/Ag sandwiched joint", Metallurgical Transactions A, Vol. 19 A, March 1988, pp. 675 – 686.

31. W. D. MacDonald, and T.W. Eager, "Transient liquid phase bonding", Annual Review of Material Science, Vol. 22, 1992, pp. 23-46.

32. Y. Zhou, W.F. Gale, and T. H. North, "Modeling of transient liquid phase bonding", International Materials Review, Vol. 40, No.5, 1995, pp.181- 196.

33. K. Nakagawa, C. H. Lee and T. H. North, "Modeling of base metal dissolution behavior during transient liquid phase bonding", Metallurgical Transactions A, Vol. 22A, Feb. 1991, pp. 543 – 555.